Turbulence in mobile-bed streams

Subhasish Dey[1], Ratul Das[1], Roberto Gaudio[2] and Sujit K. Bose[3]

[1]Department of Civil Engineering, Indian Institute of Technology, Kharagpur 721302, West Bengal, India; e-mail: sdey@iitkgp.ac.in (corresponding author); ratuliitkgp@gmail.com

[2]Dipartimento di Difesa del Suolo "V. Marone", Università della Calabria, 87036 Rende (CS), Italy; e-mail: gaudio@unical.it

[3]Centre for Theoretical Studies, Indian Institute of Technology, Kharagpur 721302, West Bengal, India; e-mail: sujitbose@yahoo.com

Abstract

This experimental study is devoted to quantify the near-bed turbulence parameters in mobile-bed flows with noncohesive bed-load sediment transport and to compare them with those in clear-water flows. A reduction in magnitude of near-bed turbulence level due to the decrease of flow velocity relative to particle velocity transporting particles results in an excessive near-bed damping in Reynolds shear stress (RSS) distributions. The bed particles are associated with the momentum provided from the flow to maintain their motion overcoming the bed resistance. It leads to a reduction in RSS distributions over the entire flow depth. In the logarithmic law, the von Kármán coefficient decreases, and the virtual bed and the zero-velocity levels move up in presence of bed-load transport. The friction factor decreases with bed-load transport substantiating the concept of reduction of flow resistance. The traversing length of an eddy decreases and its size increases in mobile-bed flows, as compared to those in clear-water flows. The third-order correlations suggest that during the bed-load transport, a streamwise acceleration inclining downward is prevalent. It is associated with a streamwise diffusion of vertical Reynolds normal stress (RNS) and a downward diffusion of streamwise RNS. The streamwise and the downward vertical fluxes of turbulent kinetic energy (TKE) increase in presence of bed-load transport. The TKE-budget reveals that for the bed-load transport the pressure energy diffusion rate near the bed changes sharply to a negative magnitude, implying a gain in turbulence production. According to the quadrant analysis, sweep events in mobile-bed flows are the principal mechanism of bed-load transport. Using a Gram-Charlier series expansion based on the exponential distribution, the universal probability density functions (PDFs) for turbulence parameters given by Bose and Dey (2010) have been successfully applied in mobile-bed flows.

Key words: flow characteristics, hydraulics, open-channel flow, sediment transport, stream beds, turbulent flow.

1. INTRODUCTION

From the perspective of geophysical hydrodynamics, events of sediment transport by the turbulent flows are of significant importance, since they govern the morphodynamical changes by entraining and depositing the sediments. Sediment transport, in fact, modifies the turbulent flow characteristics, as compared to those over an immobile-bed. The underlying mechanisms of flows over an immobile-bed and a mobile-bed are quite different in terms of the interactions of transported particles with the fluid and those with the bed. The flow acts to accelerate the particles, while the bed offers resistance to decelerate them. In this way, a considerable fraction of the momentum of the particles goes into the bed and only a part of the momentum can be recovered by the flow. The fluid energy thus transferred to the particles in motion is essentially dissipated. Over and above, the whole process in turbulent flows is highly stochastic in nature. This phenomenon gives rise to investigate the energy and momentum exchanges which are due to the sediment transport, in terms of turbulent kinetic energy (TKE) and shear stress: especially the influence of the transported particles on the TKE-budget and Reynolds shear stress (RSS) production. In this context, an attempt is made to interpret the flow measurements by making use of the concept of turbulent structures. Therefore, an investigation of this category essentially involves two modes of sediment transport. In the first mode, the bed was immobile with no sediment transport, called *clear-water flow*; and in the second, a continuous weak sediment transport (as bed-load) was established by the flow in the form of a thin layer disallowing any bed-forms development, called *mobile-bed flow*. Therefore, in both the modes, the sediment beds should remain flat and hydraulically rough with the sediment particles devoid from any bed-forms, as the presence of bed-forms could add further intricacy towards the bed-roughness and the flow characteristics as well.

The contrasting bed conditions are the cause of the different characteristics of mobile-bed flows with respect to clear-water flows. In general, the flow resistance is found to increase in mobile-bed flows and also in the presence of sediment feeding transported as bed-load over rough immobile-beds as compared to that in clear-water flows (Gust and Southard 1983, Wang and Larsen 1994, Best *et al.* 1997, Song *et al*. 1998, Calomino *et al*. 2004, Gaudio *et al*. 2011). Transport of coarse sand studied by Wang and Larsen (1994) and that of glass globules (diameter = 0.22 mm) studied by Best *et al.* (1997) showed that the bed-particle transport results in a reduction of the time-averaged streamwise velocity and an enhancement of the velocity gradient and turbulence intensities in the near-bed flow zone. These results are in conformity with the view that the collisions of bed-particles receive the kinetic energy from the time-averaged flow resulting in a near-bed momentum deficit; as a consequence, a reduction of the streamwise velocity is prevalent (Owen 1964, Smith and McLean 1977). Importantly, the particles during bed-load transport interact with the flow and the bed as well. The flow accelerates the particles, while the bed roughness retardates them until they come to a rest (Gyr and Schmid 1997). Bergeron and Carbonneau (1999) explained that the increase in flow resistance depends on the enhancement of the apparent roughness due to the withdrawal of momentum from the flow in presence of bed-load transport resulting in a reduction of time-averaged velocity. To be more explicit, sediment particles are accelerated by the flow, forming wakes and resulting in an enhancement of roughness, called *apparent roughness*. On the other hand, some studies suggested that the bed-load transport is instead to decrease the flow resistance, resulting in an increase of streamwise velocity. For instance, Nikora and Goring (2000) reported that the weak gravel transport as a bed-load in a field canal is the cause to increase the streamwise velocity. Carbonneau and Bergeron (2000) reported that the bed-load transport causes an increase in velocity, demonstrating that the effect of sediment transport on mean flow characteristics is rather complex. Campbell *et al.* (2005), who used the double-averaging method (DAM) (Nikora *et al.* 2001), observed a decrease in streamwise velocity in mobile-bed flows for larger particles, as compared to that in clear-water flows, but their observation for smaller particle size was quite opposite. In an attempt with the DAM by Radice and Ballio (2008), it was shown that considering the intermittency of the sediment transport process, it could be possible to interpret the double-averaged particle velocity being directly proportional to the shear velocity. There are also some studies suggesting a little influence of the sediment mobility on the flow resistance. Pitlick (1992) observed that the developing bed-forms induce an increased flow resistance, but the weak bed-load transport over a flat gravel-bed affects little. Yang and Hirano (1995) found that the flow resistance is not influenced by the bed-load transport. Regarding the universality of the *von*

Kármán coefficient κ, Gust and Southard (1983) and Bennett *et al.* (1998) for smooth and transitional regimes and Bennett and Bridge (1995), Nikora and Goring (1999), Gallagher *et al.* (1999) and Dey and Raikar (2007) for full-rough regime reported a decrease in κ from its universal value due to the bed mobility; whereas Gyr and Schmid (1997) for smooth regime and Song *et al.* (1994) for fully-rough regime did not confirm this aspect. Gaudio *et al.* (2010) presented a review on the non-universality of κ in fluvial streams. Regardless of whether the bed-load transport acts to increase or decrease or has a negligible effect on flow resistance, it is confirmed that the mean flow and turbulence parameters of a mobile-bed flow differ significantly from those of a clear-water flow. However, the up-to-date knowledge on the potential differences is still limited and relates to rather narrow ranges of controlling parameters and experimental situations. There are also some issues related to the turbulent flow structures and events, which require adequate clarifications and are discussed as follows:

Researches on the turbulent wall-layers corroborate that the near-wall flow is characterized by a sequence of turbulent bursting events (Kline *et al.* 1967, Robinson 1991). It represents the governing mechanism of TKE-production near the wall (Nezu and Nakagawa 1993). Turbulent bursting cycle comprises of a sequence of quasi-cyclic process of low speed fluid parcel ejected (called *ejection events*) from the near-wall zone and subsequent high speed fluid parcel sweeping (called *sweep events*) as an inrush of the slowly moving fluid left from the preceding ejection events. Bursting events therefore play an important role in transporting sediments. Thus, the breakthrough of the bursting phenomenon in turbulent wall-layers has created an enthusiasm in further studying the structure of near-wall flows for an advanced knowledge to explore the problem of sediment transport. The role of the coherent turbulent structures on the bed-load transport was investigated by Heathershaw and Thorne (1985) in tidal channels. They pointed out that the bed-load transport is not correlated with the instantaneous RSS, but it can be correlated with the near-wall instantaneous streamwise velocity. Field observations on transport of gravels by Drake *et al.* (1988) revealed that the gravel transport is associated with sweep events. These events occur for a short fraction of time at any particular location of the bed, making the transport process rather episodic, with short periods of high transport rate intermingled with long periods of relatively negligible transport rate. In an effort to correlate the turbulence characteristics with the sediment mobility, some researchers proposed the RSS components being not the most relevant parameter defining the sediment transport (Clifford *et al.* 1991, Nelson *et al.* 1995). Best (1992) attempted to correlate the sweeps with the sediment transport and bed defect (bed perturbation) by using the hydrogen bubble visualization. Field investigations by Nikora and Goring (2000) suggested that the characteristics of turbulence in flows over weakly mobile-beds could be different from those over immobile-beds and beds with intense bed-load transport. The studies by Krogstad *et al.* (1992) and Papanicolaou *et al.* (2001) further evidenced that the bed packing conditions in gravel bed streams affect the turbulence characteristics of the flow, and as a result, the sediment movement. In this context, it is pertinent to point out that the analysis of bursting events by Papanicolaou *et al.* (2001) showed that the ratio of the RSS to the streamwise turbulence intensity is smaller in the low-densely packed beds than in the densely packed beds. Hence, sediment transport criterion based on the time-averaged bed shear stress may under-predict, especially for the low-densely packed beds. Sumer *et al.* (2003) studied the role of externally induced turbulence fields on the bed-load transport and argued that the sediment transport rate increases considerably with an increase in turbulence level. Recently, Dey *et al.* (2011) studied the influence of turbulent events on the initiation of sediment motion. They observed that the sweep events are the key mechanism of initiation of sediment motion.

Despite number of serious efforts, the relative role of the mean flow and turbulence characteristics on the sediment dynamics has yet to be ascertained. This study therefore addresses how the turbulence characteristics in flows respond to bed-load transport of noncohesive sediments. It provides important results pertaining to the turbulence characteristics, such as RSS, time-averaged velocity, mixing-length and Taylor microscale, third-order correlations, TKE-flux, TKE-budget, bursting events and probability density functions (PDFs) of turbulence parameters. Experiments were conducted in absence of bed-forms. Analysis of experimental data, measured by an acoustic Doppler velocimeter (*Vectrino* probe) with sampling frequency of 100 Hz, in clear-water and mobile-bed flows, allows understanding the modifications in the mean flow and turbulence parameters due to difference in bed conditions. Here, the experimental data for clear-water flows are used as a reference. This study is in fact the extension of the study done by Dey *et al.* (2011) on threshold-bed flows to fully mobile-bed flows.

2. EXPERIMENTAL ARRANGEMENTS AND PROCEDURE

The study was conducted in the Hydraulic and Water Resources Engineering Laboratory at the Department of Civil Engineering, Indian Institute of Technology, Kharagpur, India. A rectangular open-channel flume with glass-walls was used for the experiments [Fig. 1(a)]. It was 0.91 m wide, 0.71 m deep and 12 m long. A sediment feeder operated by an electro-mechanical device was installed at the inlet of the flume to feed sediments into the flow. It had a hopper and a conveyer belt, as main components. A speed-regulator for the rollers that drove the conveyer belt carrying sediments regulated the sediment feeding at a uniform rate. Fig. 1(b) shows the photograph of the sediment feeder apparatus. The inflow rate was controlled by a valve and measured by a calibrated V-notch weir. The flow depth was controlled by an adjustable tailgate at the flume outlet and measured by the point gauges. Three uniformly graded sediments were used for the experiments, with median diameters d_{50} = 0.95, 2.6 and 4.1 mm, respectively. The geometric standard deviations of the particle size distributions $\sigma_g = (d_{84}/d_{16})^{0.5}$ were always less than 1.3, where d_{16} and d_{84} are the particle sizes finer than 16 and 84% by weight, respectively. The characteristics of the sediment samples used for the experiments are shown in Table 1.

For each sediment sample, an experimental set comprised of two different runs for clear-water and mobile-bed flow conditions. Utmost care was taken to ensure that the immobile-bed roughness became unchanged throughout the experiments for a sediment sample. To prepare an immobile-bed, synthetic glue was sprayed on the surface of the flume bottom and then the sediments were spread uniformly by means of a sieve to create a rough-bed. Care was taken not to flood the surface by the glue. After completely drying, the bed surface was brushed before commencing an experiment. In each experimental set, the clear-water flow structure over the immobile-bed with no sediment transport was first measured. Then, the mobile-bed flow structure was measured during the bed-load transport of sediments at a certain rate corresponding to the same flow condition as that of the clear-water flow. The sediment was fed into the flow at a uniform rate through a hopper and a conveyer belt attached to a gearing system, as shown in Fig. 1(b). The sediment transport capacity of the flows always equaled or exceeded the bed-load feeding rates. Thus, the bed-load transport rate was approximately balanced by the feeding rate, leading to a dynamic equilibrium. The feeding sediments were transported, forming a thin layer as a pure bed-load with particles rolling rather than saltating, as visually observed. Occasionally, for sediment feeding with size 4.1 mm, particles had a tendency to become temporarily lodged on the localized zone of the bed, but they traveled after a short while. In this way, sediments were transported right towards the flume outlet without developing bed-forms or deposition. The sediments transported by the flows were collected in a downstream box, called sediment collector.

Three different streamwise bed-slopes S = 0.13, 0.30 and 0.38% were used for d_{50} = 0.95, 2.6 and 4.1 mm, respectively. The experiments were conducted under a uniform flow. It was ensured by measuring the flow depths within the reach from 6 to 9 m (from the flume inlet), within which the flow measurement was done. The ranges of relative submergence S_h (= d_{50}/h, where h is the flow depth), flow Reynolds number R (= $4hU/\upsilon$, where U is the depth-averaged velocity and υ is the kinematic viscosity of fluid considered as 10^{-6} m^2/s) and flow Froude number F [= $U/(gh)^{0.5}$, where g is the gravitational acceleration] were studied as $6.33\times10^{-3} \leq S_h \leq 3.42\times10^{-2}$, $2.38\times10^5 \leq R \leq 5.51\times10^5$ and $0.55 \leq F \leq 0.77$, respectively. The experimental conditions were independent of S_h, as the values of S_h were far below 0.1. The shear-particle Reynolds numbers R_* (= $d_{50}u_*/\upsilon$, where u_* is the shear velocity) were in general close to or greater than 70. Thus, the flow conditions were rough-turbulent.

A four-receiver acoustic Doppler velocimeter probe, named *Vectrino* (manufactured by Nortek), working with an acoustic frequency of 10 MHz was used to measure the instantaneous velocity components. A sampling rate of 100 Hz was used for the data acquisition. The sampling volume was cylindrical, having 6 mm diameter and an adjustable height varying from 1 to 4 mm. Within the wall-shear layer of flow (within 20% of flow depth), the sampling height was set as 1 mm. On the other hand, above the wall-shear layer of flow (above 20% of flow depth), the sampling height was used as 4 mm. The closest measuring location to the bed was always 2 mm from the bed surface. Duration of sampling 300 s was found to be adequate to achieve the statistically time-independent averaged velocity and turbulence quantities (including third-order correlations and TKE-fluxes). The measurement within top 5 cm of the flow layer could not be performed due to the limitation of the probe. The flow measurements were performed along the vertical over the centerline at a distance of 7.5 m from the inlet. Such an arrangement ensured to avoid transverse gradients of velocity, if there was any. Further, as far as the flow three-dimensionality is concerned, owing to the fact that the aspect ratios (that is the ratio of flume width to flow depth) were greater than 6, the flows in all the experiments were free from any three-dimensional effect induced by the side-walls (Yang *et al.* 2004). The *Vectrino* data uncertainty, given in Table 2, was determined by testing 12 samples collected at a rate of 100 Hz over a period of 300 s. These samplings were taken at a location of 3 mm over the beds formed by the sediment sizes of d_{50} = 0.95 and 4.1 mm. In Table 2, u', v' and w' are the fluctuations of instantaneous streamwise velocity u, spanwise velocity v and vertical velocity w, respectively, $(\overline{u'u'})^{0.5}$ is the root-mean-square (rms) of u', $(\overline{v'v'})^{0.5}$ is the rms of v', $(\overline{w'w'})^{0.5}$ is the rms of w', and $-\overline{u'w'}$ is the RSS divided by the mass density ρ of fluid. To avoid the bias and the random errors of the experimental setup, samplings were taken at different times after resuming the experiments. The data shown in Table 2 are within ±5% error for the time-averaged velocities and rms quantities and within ±8% error for the RSS, corroborating the capability of 100 Hz frequency of measurements by *Vectrino*. Table 3 provides the important experimental parameters of different sets. In a mobile-bed flow, the shear velocities u_{*S} [= $(ghS)^{0.5}$] determined from the bed slope were always greater than the shear velocities $u_{*\tau}$ [= $(-\overline{u'w'})^{0.5}\big|_{z=0}$] obtained from the RSS measurements. The notation $u_{*\tau}$ is henceforth replaced by u_*. The reason of the discrepancy in shear velocities for clear-water and mobile-bed flows is discussed in section 3. Regarding the coordinate system, the bed surface is the reference of the z-axis (z = 0), being positive in the normally upward direction. The x-axis is aligned with the bed surface (along the centerline of the flume), being x = 0 at the measuring location and positive in the streamwise direction. The transverse axis is y, being positive in the right (right-hand rule). Therefore, the measuring location has coordinates (0, 0, z).

In all experiments, the signal-to-noise ratio was maintained 15 or above. The signal correlations between transmitted and received pair of pulses were in general greater than 70%, which was the recommended cut-off value. However, on a number of occasions, the signal correlations close to the bed were dropped down by approximately 5% from its recommended cut-off value due to potentially steep velocity gradient within the sampling volume. The data measured by the *Vectrino* in the near-bed flow zone contained spikes resulting from the interference between incident and reflected pulses. So, the data were filtered by a spike removal algorithm based on the *acceleration thresholding method* (Goring and Nikora 2002). This method was capable in detecting and replacing spikes in two phases. The threshold values (= 1 – 1.5) for despiking were chosen (by trial and error) in such a way so that the velocity power spectra provided an acceptable fit with Kolmogorov "–5/3 scaling-law" in the inertial subrange (Lacey and Roy 2008). Using the discrete fast Fourier transforms, the velocity power spectra $F_{ii}(f)$ were calculated, where f is the frequency. Figs. 2(a and b) present $F_{ii}(f)$ at z = 0.005 m in clear-water and mobile-bed flows before and after spike removal. The power spectra of despiked signals display a satisfactory agreement with Kolmogorov "–5/3 scaling-law" in the inertial subrange of frequency that occurs for frequencies $f > 1$ Hz. These features corroborate the adequacy of the *Vectrino* measurements in clear-water and mobile-bed flows. The power spectra exhibit similar relationships between the velocity components, where $F_{uu} \approx F_{vv} > F_{ww}$. It is however evident that discrete spectral peak was not observed for $f > 0.5$ Hz. It implies that the signals for $f \leq 0.5$ Hz contained large-scale motions; while those for $f > 0.5$ Hz had pure turbulence. The raw measured data were therefore decontaminated by using a high-pass filter with a cut-off frequency of 0.5 Hz, correlation threshold and spike removal algorithm. The difference in power spectra $F_{ii}(f)$ for clear-water and mobile-bed flows is not apparent. Therefore, the spectra were not contaminated by the transported sediments. In this context, it is pertinent to mention that Best *et al*. (1997) quantified a cross-talk between fluid and suspended sediment particles to yield errors of between ±0.05 to 0.8% in time-averaged velocity and ±0.3 to 3.3% in rms of velocity fluctuations measured by a phase Doppler anemometer. As there were no suspended sediments in the present study, the measured data were free from any cross-talk. In addition, four-receiver *Vectrino* system had a redundancy for the vertical velocity components, since w_1 and w_2 were simultaneously measured, where subscripts "1" and "2" refer to the vertical components measured by two beams. The noise estimation for a four-receiver system was performed by the method given by Blanckaert and Lemmin (2006) for the despiked data. The variance σ_z^2 of the noise is given by

$$\sigma_z^2 = \frac{\sigma_{z1}^2 + \sigma_{z2}^2}{2} \tag{1}$$

where $\sigma_{z1}^2 = \overline{w_1' w_1'} - \overline{w_1' w_2'}$, and $\sigma_{z2}^2 = \overline{w_2' w_2'} - \overline{w_1' w_2'}$. It was considered that data having $\sigma_z^2 < 0.3\,\overline{w_1' w_2'}$ were noise-free, as they corresponded well to the signal correlations greater than 70.

3. RSS DISTRIBUTIONS

Fig. 3(a) presents the vertical distributions of nondimensional RSS $\hat{\tau}(\hat{z})$ for all the runs for clear-water and mobile-bed flows. The RSS τ (= $-\rho\overline{u'w'}$) is scaled by the bed shear stress τ_0 (= ρu_*^2) and the vertical distance z by the flow depth h. Here, $\hat{\tau}$ is τ/τ_0 and $\hat{z}$ is z/h. In the flow-layer $\hat{z} > 0.1$, the data plots for both the cases collapse on the linear law of RSS (also termed gravity line), $\hat{\tau} = 1 - \hat{z}$, for the free surface flows with a zero-pressure gradient. Near the bed, the $\hat{\tau}$-distributions suffer from a damping that is apparent from a departing band of data plots from the linear law. The damping in τ-distributions close to the rough-bed is a common feature due to the formation of roughness sub-layer that gives rise to form induced stress (Sarkar and Dey 2010). Nevertheless, an excess damping in τ-distributions for mobile-bed flows over that in clear-water flows is noticeable, which is an important aspect to be explored in the context of bed-load transport. This damping is attributed to the fact that the particles on motion result in a reduction in flow velocity relative the particle velocity to drag them. To be more explicit, initially particles are dragged by the flow from the rest and then accelerate, while the resistance at contacts of bed particles retards them. In this way, a dynamic equilibrium is established, when the particles in motion require overcoming only the frictional resistance from the bed. Thus, the resulting wakes produce a lesser turbulence level in mobile-bed flows than in clear-water flows. It is to be noted that the clear-water flows in this study were the forced ones, as the sediment particles were glued. Otherwise, they would have had motion by the same flow. In Table 3, for clear-water flows, the values of shear velocity u_{*s} obtained from the bed slopes correspond well with those of $u_{*\tau}$ obtained from the τ-distributions. In contrast, for mobile-bed flows, the values of u_{*s} are consistently greater than those of $u_{*\tau}$. It implies that the mobility of sediment particles influences the τ-distributions over the entire flow depth, as $u_{*\tau}$ [$= (-\overline{u'w'})^{0.5}\big|_{z=0}$, denoted by u_*] is determined from the linear projection of a τ-distribution onto the bed. The decreased magnitude of u_* for mobile-bed flows is thus attributed to a portion of the RSS transmitted to the bed particles to prevail over the resistance at the contacts of the transported sediment particles. An analogous concept of Grass (1970) supports this phenomenon. The reduction in magnitude of u_* and thus in τ-distributions can also be clarified observing that the bed particles are associated with the momentum provided from the flow to maintain their motion (Yeganeh-Bakhtiary *et al.* 2000, 2009). The relative difference in τ between clear-water (subscript "*cw*") and mobile-bed (subscript "*mb*") flows can be estimated by $\Delta\tilde{\tau} = 1 - (\tau)_{mb}/(\tau)_{cw}$. Fig. 3(b) shows the variation of $\Delta\tilde{\tau}$ with $\hat{z}$ for all the runs. It is evident that the difference in τ in the near-bed zone becomes as high as $0.7(\tau)_{cw}$. Sumer *et al.* (2003), who studied the bed-load transport under externally induced turbulence fields, argued that the sediment transport rate increases with turbulence level. In contrast, the present study puts forward an argument that the sediment transport is associated with a reduction in the turbulence level in a wall-shear flow, as compared to clear-water flows. It implies that both the arguments are true, as an increased turbulence is the cause to increase the transport rate, but the turbulence level reduces in presence of bed-load transport. In conclusions, two important issues comes out from the analysis of RSS distributions: (1) a near-bed damping in RSS distributions results from a lesser magnitude of turbulence level in mobile-bed flows being in excess of that in clear-water flows; and (2) a reduction in RSS distributions over the entire flow depth in mobile-bed flows results from the bed particles that are associated with the provided momentum from the flow to maintain their motion overcoming the bed resistance.

4. TIME-AVERAGED VELOCITY DISTRIBUTIONS

Fig. 4(a) shows the vertical distributions of nondimensional time-averaged streamwise velocity u^+ for all the runs for clear-water and mobile-bed flows. In order to fit the data points in the inner-layer ($z \leq 0.2h$) to the universal logarithmic law of wall (log-law), the time-averaged streamwise velocity $\bar{u}$ and the vertical distance z are scaled by u_* and d_{50}, such that $u^+ = \bar{u}/u_*$, and $z^+ = z/d_{50}$. As the flow regime was the rough-turbulent flow, it is customary to use d_{50} scaling z. Since the primary focus of this study is on the role of turbulence characteristics, the values of u_* (= $u_{*\tau}$) are preferred to those of u_{*s}. Moreover, the τ-distributions provide the truly available turbulent shear stress in the flowing fluid and so $u_{*\tau}$ is chosen as shear velocity. To plot the experimental data, we consider the log-law as expressed in following nondimensional form:

$$u^+ = \frac{1}{\kappa}\ln\left(\frac{z^+ + \Delta z^+}{\zeta^+}\right) \tag{2}$$

where κ = von Kármán coefficient, $\Delta z^+ = \Delta z/d_{50}$, Δz = depth of the virtual bed level from the bed surface, $\zeta^+ = z_0/d_{50}$, and z_0 = zero-velocity level. Fig. 4(a) describes the log-law showing variations of u^+ with $z^+ + \Delta z^+$ for the experimental datasets. It is clear that a prior estimation of Δz^+ was an essential prerequisite to plot the data, and subsequent determination of κ and ζ^+ was required to fit the data to the log-law given by eq. (2). The determination of these parameters was done independently, as described below:

Step 1: Having obtained u_* from the τ-distributions as $u_* = (-\overline{u'w'})^{0.5}\big|_{z=0}$, prepare the data $u^+(z^+)$ for the range of $z \leq 0.2h$ for the analysis.

Sept 2: As an initial trial, considering $\Delta z^+ = 0$, determine κ and ζ^+ from eq. (2) by the regression analysis and evaluate the regression coefficient, *RC*.

Sept 3: Increase Δz^+ at a regular interval by a small magnitude (say 0.001) and determine κ and ζ^+ in the same way as given in step 2, and check *RC* for each value of Δz^+, till *RC* becomes maximum. Then, the corresponding values of Δz^+, κ and ζ^+ are the determined parameters for eq. (2).

The values of Δz^+, κ and ζ^+ obtained for all the runs are furnished in Table 3. It is obvious that the values of κ for mobile-bed flows drop from its traditional universal value ($\kappa = 0.41$), while those for clear-water flows preserve the traditional constant value. It is in conformity with those obtained by previous researchers for flows with bed-load transport (Bennett and Bridge 1995, Nikora and Goring 1999, Gallagher *et al.* 1999, Dey and Raikar 2007, Gaudio *et al*. 2011). The average values of $\Delta z^+ = 0.39$, $\kappa = 0.413$ and $\zeta^+ = 0.034$ for clear-water flows are in agreement with those for the traditional log-law over rough beds. Typically, the customary values of the parameters for the rough beds are $\Delta z^+ = 0.25$, $\kappa = 0.41$ and $\zeta^+ = 0.033$ (van Rijn 1984). Thus, for clear-water flows, the data collapse well on the average log-law curve given by a solid line in Fig. 4(a) and the corresponding errors shown in Fig. 4(b) are well below ±10%. On the other hand, the average values of $\Delta z^+ = 0.21$, $\kappa = 0.37$ and $\zeta^+ = 0.04$ for mobile-bed flows suggest the modified values of the parameters for the log-law over rough mobile-beds. It is obvious that for mobile-bed flows, the data exhibit some degree of scatter about the average log-law curve [Fig. 4(a)]. Nevertheless, the corresponding errors shown in Fig. 4(b) are within ±10%. Importantly, if we use the values of the parameters from Table 3 for an individual run, then the matching between the experimental data and the log-law would be excellent. A comparison of the values of Δz^+ and ζ^+ for clear-water and mobile-bed flows reveals that the virtual bed and zero-velocity levels move up in presence of bed-load transport. Although the analysis related to the log-law was done considering the data range of $z \leq 0.2h$, Fig. 4(a) displays all the data (for $z \leq 0.2h$ and $z > 0.2h$) plots. Thus, the data plots depart in the outer-layer to some extent. However, Fig. 4(b) includes only the data for $z \leq 0.2h$ to demonstrate the errors in log-law fittings. Additionally, the estimates of the friction factor λ (= $8u_*^2/U^2$) are furnished in Table 3. Fig. 5 presents the data plots of λ versus h/ε for all the runs for clear-water and mobile-bed flows, where ε is the Nikuradse equivalent sand roughness. Both the plots for λ_s and λ_τ obtained from bed slope and RSS are shown. The values of ε were determined from the relationship for zero-velocity level as $\varepsilon = 30\zeta^+ d_{50}$. The data plots are also compared with the empirical curve given by Song *et al.* (1998) for clear-water flows. It is evident that the data points for clear-water flows lie around the empirical curve. However, the values of λ for mobile-bed flows decrease with respect to those for clear-water flows and with an increase in h/ε, as data points encircled in Fig. 5. Therefore, the reduction of resistance in presence of bed-load transport is again substantiated. Hence, the finding for mobile-bed flows by Song *et al.* (1994, 1998), who argued that the bed friction factor λ increases with bed-load transport, is in contradiction with the present results. They calculated u_* from the bed slopes. The calculation of u_* from the bed slopes is valid only for the clear-water flows and cannot truly predict u_* for mobile-beds, since the original derivation of u_* is based on the fluid force balance on a rigid wall. However, for an experiment in a narrow channel having aspect ratio << 6, as the wall induced secondary-currents form cells increasing the flow resistance, the sediment feeding to simulate bed-load transport over a rough immobile-bed could result in an increase of bed resistance to the main flow (Calomino *et al*. 2004, Gaudio *et al*. 2011). Finally, it can be concluded that for mobile-bed flows, (1) von Kármán coefficient and friction factor (or frictional resistance) decrease and (2) virtual bed and zero-velocity levels move up.

5. PRANDTL MIXING-LENGTH AND TAYLOR MICROSCALE DISTRIBUTIONS

According to Prandtl, the mixing-length l, which defines a distance that a fluid parcel (eddy) keeps its original characteristics before dispersing into the surrounding fluid, is given by

$$l = \frac{(-\overline{u'w'})^{0.5}}{d\bar{u}/dz} \tag{3}$$

To calculate the mixing-length l from eq. (3), the measured velocity profiles were used to determine the velocity gradients $d\bar{u}/dz$ by smooth curve fitting to the data, and the values of $-\overline{u'w'}$ were obtained directly from the measured RSS distributions. The variations of nondimensional mixing-length $\hat{l}$ (= l/h) with $\hat{z}$ for Runs 6a and 6b are shown in Fig. 6. Within the inner-layer ($z \leq 0.2h$) of wall-shear, $\hat{l}$ varies linearly with $\hat{z}$ and all the experimental data points for clear-water and mobile-bed flows collapse reasonably on a single band, which is in conformity with the Prandtl's hypothesis. Also, data points collapse satisfactorily on the curves obtained from the theoretical equation $\hat{l} = \kappa\hat{z}(1 - \hat{z})^{0.5}$ given by Nezu and Nakagawa (1993). The slope of the linear portion defining κ (= $\hat{l}/\hat{z}$ = l/z) for mobile-bed flows is smaller than that for clear-water flow. It suggests that the traversing length of an eddy decreases with bed-load transport and increases more rapidly with z in clear-water flows. It is another confirmation towards the reduction of mobile-bed resistance to flow.

Studies done by Gore and Crowe (1991), Hetsroni (1993), Crowe (1993), Best *et al.* (1997) argued that in flows with transported particles, the ratio of the size of transported particles to the length scale of turbulence is involved in influencing the enhancement or attenuation of the streamwise turbulence intensity. Taylor microscale λ_T, that defines the eddy size in the inertial subrange, is the relevant length scale of turbulence, given by

$$\lambda_T = \left(\frac{15\upsilon\sigma_u^2}{\varepsilon}\right)^{0.5} \quad (4)$$

where σ_u = streamwise turbulence intensity, that is $(\overline{u'u'})^{0.5}$, and ε = TKE-dissipation rate. The estimation of ε is done by using Kolmogorov's second hypothesis that predicts the following equality describing the true inertial subrange (Pope 2001):

$$k_w^{5/3} S_{uu} = C\varepsilon^{2/3} \quad (5)$$

where k_w = wave number, $S_{uu}(k_w)$ = spectral density function for u', and C = constant approximately equal to 0.5 (Monin and Yaglom 2007).

In Fig. 7(a), the spectra $S_{uu}(k_w)$ [= $(0.5\overline{u}/\pi)F_{uu}(f)$] as a function of k_w [= $(2\pi/\overline{u})f$] are drawn using the despiked instantaneous velocity data. The inertial subranges in clear-water and mobile-bed flows are satisfactorily characterized by Kolmogorov "–5/3 scaling-law". It corresponds to a subrange of k_w where the average value of $k_w^{5/3}S_{uu}$ is relatively constant (that is independent of k_w), as shown in Fig. 7(b). Then, ε was estimated from eq. (5) and λ_T was from eq. (4). Fig. 8(a) shows the variations of the ratio of sediment size to Taylor microscale, that is $\hat{\lambda}_d = d_{50}/\lambda_T$, with $\hat{z}$

for Runs 6a and 6b. Near the bed ($z \leq 0.1h$), $\hat{\lambda}_d$ for mobile-bed flows is smaller than that for clear-water flows. In the outer-layer, $\hat{\lambda}_d$ for both the cases being almost same decreases away from the bed. The values of λ_T near the bed are 2 and 2.44 mm in clear-water and mobile-bed flows, respectively. Hence, the eddy size close to the bed increases in presence of bed-load transport. Previous studies on two-phase flows reported that the range of $\hat{\lambda}_d \approx 0.2$ to 1.2 corresponds to the turbulence enhancement; while the range of $\hat{\lambda}_d \approx 0.2$ to 0.065 corresponds to the turbulence attenuation (Gore and Crowe 1991, Hetsroni 1993, Best *et al*. 1997). Fig. 8(b) presents the data plots of $\hat{\lambda}_d$ for mobile-bed flows as a function of relative difference of streamwise turbulence intensities $\Delta\sigma_u$ [= $(\sigma_u)_{mb}/(\sigma_u)_{cw} - 1$] for Runs 6a and 6b. The results are in agreement with those obtained by the previous investigators.

6. DISTRIBUTIONS OF THIRD-ORDER CORRELATIONS

Third-order correlations that carry stochastic information on the characteristics of u' and w' in terms of flux and diffusion of the turbulent stresses are attributed to the turbulent coherent structures, owing to the preservation of their signs. The set of third-order correlations is given by $M_{jk} = \overline{\hat{u}^j \hat{w}^k}$ for $j + k = 3$, where $\hat{u} = u'/(\overline{u'u'})^{0.5}$, and $\hat{w} = w'/(\overline{w'w'})^{0.5}$ (Raupach 1981). The skewness of u' is M_{30} (= $\overline{\hat{u}^3}$), defining the streamwise flux of the streamwise Reynolds normal stress (RNS) $\overline{u'u'}$. A similar expression can be written for M_{03} (= $\overline{\hat{w}^3}$), defining the vertical flux of vertical RNS $\overline{w'w'}$. On the other hand, the diffusion factors are M_{21} (= $\overline{\hat{u}^2\hat{w}}$) and M_{12} (= $\overline{\hat{u}\hat{w}^2}$), characterizing the diffusions of $\overline{u'u'}$ in z-direction and $\overline{w'w'}$ in x-direction, respectively.

Fig. 9 presents the vertical distributions of $M_{jk}(\hat{z})$ for Runs 6a and 6b. The correlation between M_{jk}-distributions for clear-water flow is $M_{30} = -2.16M_{21} = 1.93M_{21} = -1.77M_{03}$ that corresponds closely to $M_{30} = -2.02M_{21} = 1.97M_{21} = -1.7M_{03}$ as obtained by Raupach (1981). The influence of the bed-load transport on M_{jk}-distributions is evident within the near-bed flow zone. In the clear-water flow, M_{30} and M_{12} start with small negative values near the bed and decrease (increase of negative magnitudes) with $\hat{z}$. On the other hand, in the mobile-bed flow, M_{30} and M_{12} start with small positive values near the bed, changing over to negative values for $\hat{z} \geq 0.06$. It suggests that the bed-load transport influences M_{30} and M_{12} by changing the $\overline{u'u'}$-flux and the $\overline{w'w'}$-diffusion to the streamwise direction; while they (possessing feeble magnitudes) propagate against the streamwise direction in the clear-water flow. Away the bed ($\hat{z}$ > 0.06), the $\overline{u'u'}$-flux and the $\overline{w'w'}$-diffusion occur against the streamwise direction and become pronounced with an increase in $\hat{z}$ for both clear-water and mobile-bed flows. The trends of $M_{03}(\hat{z})$ and $M_{21}(\hat{z})$ in the clear-water flow are positive over the entire flow depth; whilst those in mobile-bed flows are negative near the bed ($\hat{z} \leq 0.06$) and positive for $\hat{z} > 0.06$. It suggests that the $\overline{w'w'}$-flux and the $\overline{u'u'}$-diffusion are in upward direction over the entire flow depth for the clear-water case, whereas those are in downward direction in the near-bed flow zone for the mobile-bed case. The responses of the bursting events can be reasonably obtained from the third-order correlations, although some of them remain implicit, owing to the averaging process (Nakagawa and Nezu 1977). Near the bed, the positive M_{30} and the negative M_{03} imply a strong inrush of fluid parcel in mobile-bed flow. In contrast, in the away-bed flow zone, the negative M_{30} and the positive M_{03} suggest the arrival of low-speed fluid parcel. Besides, the positive M_{12} and the negative M_{21} in near-bed flow zone imply that the bed-load transport corresponds to the $\overline{w'w'}$-diffusion in the streamwise direction and the $\overline{u'u'}$-diffusion in the downward direction. Therefore, the analysis of third-order correlations confirms that during the bed-load transport, a streamwise acceleration is prevalent and associated with a downward flux giving rise to sweeps.

7. TKE-FLUX COMPONENTS AND BUDGET DISTRIBUTIONS

The vertical distributions of nondimensional streamwise and vertical TKE-flux components F_{ku} [$= f_{ku}/u_*^3$; where $f_{ku} = 0.5(\overline{u'u'u'} + \overline{u'v'v'} + \overline{u'w'w'})$] and F_{kw} [$= f_{kw}/u_*^3$; where $f_{kw} = 0.5(\overline{u'u'w'} + \overline{v'v'w'} + \overline{w'w'w'})$] in Runs 6a and 6b are shown in Fig. 10. In the clear-water flow, the F_{ku} starts with a small negative value and decreases (increase of negative value) with $\hat{z}$. It implies that the F_{ku} transports against the streamwise direction over the entire flow depth. The inertia of flowing fluid layer induces a retarding effect being attributed to the negative value of F_{ku}. On the other hand, the positive F_{kw} over the entire flow depth suggests an upward transport of F_{kw}. Therefore, the negative F_{ku} and the positive F_{kw} compose a retardation process with the arrival of slowly moving fluid parcel. The influence of bed-load transport is prominent in the F_{ku}- and F_{kw}-

distributions. In the mobile-bed flow, the positive F_{ku} and the negative F_{kw} in the near-bed flow zone ($\hat{z} \leq 0.06$) imply the streamwise and downward transport of TKE-flux components, respectively. However, in the away-bed flow zone ($\hat{z} > 0.06$), the behavioral characteristics of F_{ku} and F_{kw} for mobile-bed flow are similar to those for clear-water flow. Therefore, the most significant characteristic of a mobile-bed flow lies on the near-bed flow zone, in which the positive F_{ku} and the negative F_{kw} compose an accelerating effect as an inrush of fluid parcel.

The TKE-budget for a uniform open-channel flow is given as follows (Nezu and Nakagawa 1993):

$$\underbrace{-\overline{u'w'}\frac{\partial \overline{u}}{\partial z}}_{t_P} = \varepsilon + \underbrace{\frac{\partial f_{kw}}{\partial z}}_{t_D} + \underbrace{\frac{1}{\rho}\cdot\frac{\partial}{\partial z}(\overline{p'w'})}_{p_D} - \underbrace{\upsilon\frac{\partial^2 k}{\partial z^2}}_{v_D} \tag{6}$$

where t_P = TKE-production rate, t_D = TKE-diffusion rate, p_D = pressure energy diffusion rate, v_D = viscous diffusion rate, p' = pressure fluctuations, and k = TKE, given by $0.5(\overline{u'u'} + \overline{v'v'} + \overline{w'w'})$. In this study, the viscous diffusion rate v_D is negligible due to large flow Reynolds numbers. The method of determination of TKE-dissipation rate ε by using eq. (5) has already been discussed in section 5. Hence, the pressure energy diffusion rate p_D can be calculated from eq. (6) as $p_D = t_P - \varepsilon - t_D$. The nondimensional parameters of TKE-budget are T_P, E_D, T_D, P_D = $(t_P, \varepsilon, t_D, p_D) \times (h/u_*^3)$. Nezu and Nakagawa (1993) gave formulations for the TKE-production and dissipation rates as

$$T_P = \frac{1}{\kappa}\left(\frac{1-\hat{z}}{\hat{z}}\right) \tag{7}$$

$$E_D = \frac{9.8}{\hat{z}^{0.5}}\exp(-3\hat{z}) \tag{8}$$

Fig. 11 illustrates the TKE-budget in flows for Runs 6a and 6b. The TKE-production rate T_P corresponds to the conversion of energy from the time-averaged flow to the turbulence. It has near-bed amplification and decreases monotonically with an increase in $\hat{z}$ becoming nearly constant (with a small magnitude) for $\hat{z} > 0.3$. The E_D also decreases with $\hat{z}$ in the similar way as T_P varies. The distributions of E_D have a distinct lag from those of T_P. However, the curves of T_P and E_D obtained by using eqs. (7) and (8), as proposed by Nezu and Nakagawa (1993) overestimate the experimental data plots of T_P and E_D to some extent. The influence of bed-load transport is apparent in the near-bed distributions of T_P and E_D, where the lag is reduced considerably. To be explicit, the effect of sediment motion is to reduce T_P significantly and E_D weakly. The reduction of T_P in near-bed flow zone in presence of bed-load is an effect of the damping in RSS distribution. Importantly, the difference of T_P and E_D at any depth $\hat{z}$ is balanced by the summation of T_D and P_D. The T_D decreases monotonically with an increase in $\hat{z}$ within the wall-shear layer and then it becomes almost invariant of $\hat{z}$ with a small magnitude. The bed-load transport influences T_D by increasing its magnitude in comparison to T_D in clear-water flows. In the clear-water flow, P_D almost equals to E_D, but it decreases drastically with $\hat{z}$ becoming almost invariant (with a small magnitude) of $\hat{z}$ for $\hat{z} > 0.06$. The most interesting feature lies on the near-bed distributions of P_D in mobile-bed flow. It is evident that the bed-load transport is associated with a drastic changeover of P_D to a negative value ($P_D = -12$), suggesting a gain in turbulence production. It is therefore concluded that in near-bed flow zone with bed-load transport, the lag between TKE-production and dissipation rates is narrowed down and the pressure energy diffusion rate becomes negative. These findings are supported by Detert *et al.* (2010), who also reported that the bed particle motion is likely to be associated to a low-pressure flow mode.

8. CONDITIONAL RSS DISTRIBUTIONS

The characteristics of the bursting events are studied with the conditional statistics of u' and w' by plotting them on a $u'w'$-plane (Lu and Willmarth 1973). A *hole-size* parameter H categorizes the larger contributions to the RSS production from each quadrant (Nezu and Nakagawa 1993). The curves $u'(w')$ obtained from $|u'w'| = H(\overline{u'u'})^{0.5}(\overline{w'w'})^{0.5}$ define the hyperbolic hole region for a given H. Thus, the strong events (outside the hole region) and the weak events (inside the hole region) have a clear distinction depending on the value of H. The bursting events are characterized by four quadrants Qi (i = 1, 2, 3, 4): (1) *outward interactions*, $Q1$ ($i = 1$; $u', w' > 0$), (2) *ejections*, $Q2$ ($i = 2$; $u' < 0$, $w' > 0$), (3) *inward interactions*, $Q3$ ($i = 3$; $u', w' < 0$) and (4) *sweeps*, $Q4$ ($i = 4$; $u' > 0$, $w' < 0$). The contribution from the events towards the RSS production from the quadrant Qi outside the hole-size H is obtained by

$$\langle u'w' \rangle_{i,H} = \lim_{T\to\infty} \frac{1}{T} \int_0^T u'(t) w'(t) \lambda_{i,H}(z,t) dt \tag{9}$$

where T = sampling duration, t = time, and $\lambda_{i,H}(t)$ = detection function. Here, $\lambda_{i,H}(t) = 1$ if (u', w') is in quadrant Qi and if $|u'w'| \geq H(\overline{u'u'})^{0.5}(\overline{w'w'})^{0.5}$, and $\lambda_{i,H}(t) = 0$ otherwise. The quadrant analysis thus provides an estimate for the fractional contributions $S_{i,H}$ (= $\langle u'w' \rangle_{i,H} / \overline{u'w'}$) towards the RSS production from the bursting events from the quadrant i outside the hole region of size H.

To study the fractional contributions towards the RSS production from different bursting events, the data of $S_{i,H}(\hat{z})$ for $H = 0$ and 2 are plotted in Figs. 12(a and b) for Runs 6a and 6b. The high frequency events ($H = 0$) including small values associated with the use of all the pairs of u' and w' is important for the near-bed flow zone. In addition, the stronger events are studied by discarding the weaker ones for a hole-size $H = 2$ (Balachandra and Bhuiyan 2007), which corresponds to the events having greater magnitudes of RSS. Fig. 12(a) shows the vertical distributions of fractional contribution $S_{i,0}$ ($H = 0$) of the RSS in flows for Runs 6a and 6b. For the clear-water flow, $Q2$ and $Q4$ events at the nearest point of the bed contribute about 60 and 64% to the total RSS production. On the other hand, near the bed, $Q1$ events contribute minimally by 10%; while $Q3$ events contribute weakly by 14%. It suggests that the arrival of low speed fluid parcel from the near-bed flow zone is almost revoked by that of a succession high speed fluid parcel from the upper flow region. Thus, only a slowly moving process is prevalent in the form of weak $Q2$ events. In contrast, for the mobile-bed flow, $Q4$ events are the governing mechanism for bed-load transport contributing about 70% towards the RSS production; while $Q2$ events contribute relatively less (about 60%). The characteristic of $Q4$ events to dominate momentum transfer in the near-bed flow zone is therefore strongly dependent upon the transport of bed particles. It implies that the sediment motion is governed by the arrival of high speed fluid parcel. However, the contributions from $Q1$ and $Q3$ events being rather weak are about 16 and 14%, respectively. The vertical distributions of fractional contribution $S_{i,2}$ of the RSS from more extreme events occurring for hole-size $H = 2$ are given in Fig. 12(b). The most energetic $Q2$ and $Q4$ events have distinct behaviors over the entire flow depth, since the dominance of $Q4$ events for clear-water flow and that of $Q2$ events in inner region for mobile-bed flow are obvious. The divergence between $Q2$ and $Q4$ events becomes stronger. However, there remains a consensus that for both clear-water and mobile-bed flows as in Fig. 12(a), similar predominating characteristics of $Q2$ and $Q4$ events prevail, but the contributions from $Q1$ and $Q3$ events are rather trivial.

9. PDF DISTRIBUTIONS FOR TURBULENCE PARAMETERS

Flow over a rough-bed generates considerable turbulence in the near-bed flow zone. Therefore, the prevalence of bursting events in the near-bed flow zone provokes non-Gaussian PDF distributions for the turbulent quantities (Bose and Dey 2010). The instantaneous streamwise velocity u can be decomposed into a time-averaged part $\bar{u}$ and a fluctuation u', applying the Reynolds decomposition $u = \bar{u} + u'$. Owing to turbulence, the instantaneous vertical velocity w solely constitutes the fluctuations w', as the time-averaged part $\bar{w}$ remains zero, implying $w = w'$. Introducing nondimensional variables $\tilde{u}$ (= u'/σ_u) and $\tilde{w}$ (= w'/σ_w, where σ_w is the vertical turbulence intensity), Bose and Dey (2010) represented the PDF distributions for $\tilde{u}$ and $\tilde{w}$, denoted by $p_{\tilde{u}}(\tilde{u})$ and $p_{\tilde{w}}(\tilde{w})$, respectively, derived from a Gram-Charlier (GC) series expansion based on the exponential distribution as

$$p_{\tilde{u}}(\tilde{u}) = \frac{1}{2}\exp(-|\tilde{u}|) + \frac{1}{4}C_{10}\,\tilde{u}\exp(-|\tilde{u}|) - \frac{1}{16}C_{20}(1+|\tilde{u}|-\tilde{u}^2)\exp(-|\tilde{u}|)$$

$$-\frac{1}{96}C_{30}\,\tilde{u}(3+3|\tilde{u}|-\tilde{u}^2)\exp(-|\tilde{u}|) + \frac{1}{768}C_{40}(9+9|\tilde{u}|-3\tilde{u}^2-6|\tilde{u}|^3+\tilde{u}^4)\exp(-|\tilde{u}|) + \cdots \quad (10)$$

$$p_{\tilde{w}}(\tilde{w}) = \frac{1}{2}\exp(-|\tilde{w}|) + \frac{1}{4}C_{01}\,\tilde{w}\exp(-|\tilde{w}|) - \frac{1}{16}C_{02}(1+|\tilde{w}|-\tilde{w}^2)\exp(-|\tilde{w}|)$$

$$-\frac{1}{96}C_{03}\,\tilde{w}(3+3|\tilde{w}|-\tilde{w}^2)\exp(-|\tilde{w}|) + \frac{1}{768}C_{04}(9+9|\tilde{w}|-3\tilde{w}^2-6|\tilde{w}|^3+\tilde{w}^4)\exp(-|\tilde{w}|) + \cdots \quad (11)$$

The coefficients C_{j0} and C_{0k} are related to the moments m_{j0} and m_{0k} by

$$C_{10} = m_{10},\; C_{20} = \frac{1}{2}m_{20} - 1,\; C_{30} = \frac{1}{6}m_{30} - 2\,m_{10},\; C_{40} = \frac{1}{24}m_{40} - \frac{3}{2}m_{20} + 2,$$

$$C_{01} = m_{01},\; C_{02} = \frac{1}{2}m_{02} - 1,\; C_{03} = \frac{1}{6}m_{03} - 2m_{01},\; C_{04} = \frac{1}{24}m_{04} - \frac{3}{2}m_{02} + 2 \quad (12)$$

In the above equations, the moments are

$$m_{j0} = \int_{-\infty}^{\infty} \tilde{u}^j p_{\tilde{u}}(\tilde{u})\,\mathrm{d}\tilde{u}\text{, and } m_{0k} = \int_{-\infty}^{\infty} \tilde{w}^k p_{\tilde{w}}(\tilde{w})\,\mathrm{d}\tilde{w} \tag{13}$$

The coefficients C_{j0} and C_{0k} were therefore estimated from the experimental data. Thus, the relative frequency $f_{\tilde{u}}(\tilde{u})$ of the random variable $\tilde{u}$ was determined from the experimental data at a given flow depth z. Then, from eq. (13), the values of m_{j0} were estimated by approximating $p_{\tilde{u}}(\tilde{u})$ by $f_{\tilde{u}}(\tilde{u})$ and the integrals were evaluated by a composite Simpson's rule. In the similar way, the values of m_{0k} were estimated from $f_{\tilde{w}}(\tilde{w})$ of the random variable $\tilde{w}$. Hence, the C_{j0} and C_{0k} were calculated by using eq. (12); and the PDFs were estimated to draw the theoretical curves for $p_{\tilde{u}}(\tilde{u})$ and $p_{\tilde{w}}(\tilde{w})$. Figs. 13(a and b) show the $p_{\tilde{u}}(\tilde{u})$- and $p_{\tilde{w}}(\tilde{w})$-distributions closest to the bed (at z = 0.002 m) for Runs 6a and 6b. The estimated values of coefficients C_{j0} and C_{0k} and the skewness M_{30} and M_{03} are tabulated in Table 4. The experimental data correspond closely to the computed $p_{\tilde{u}}(\tilde{u})$- and $p_{\tilde{w}}(\tilde{w})$-distributions. However, the computed distributions are sharply peaked at zero-velocity fluctuations, but the corresponding experimental relative frequencies were not available for such narrow ranges in the histograms. In addition, the computed values of skewness M_{30} and M_{03} given in Table 4 are supported by those in Fig. 9. It corroborates that the PDF distributions for the velocity fluctuations derived from a GC series expansion based on the exponential distribution preserve their universality being applicable to mobile-bed flows.

For the RSS, $-\tau/\rho$ is the mean value of the product of random variable $u'w'$ whose PDF depends on the joint PDFs of u' and w'. Therefore, the random variable is $\tilde{\tau} = \tilde{u}\tilde{w}$. From this consideration, Bose and Dey (2010) derived the PDF of $\tilde{\tau}$ as

$$p_{\tilde{\tau}}(\tilde{\tau}) = K_0(2\tau_1) - \frac{1}{8}(C_{20}+C_{02})(1-\tau_1^2)K_0(2\tau_1) + \frac{1}{4}C_{11}\tilde{\tau}K_0(2\tau_1)$$

$$+\frac{1}{64}C_{22}[(1-\tau_1^2+\tau_1^4)K_0(2\tau_1) - 2\tau_1^3 K_1(2\tau_1)] - \frac{1}{96}(C_{31}+C_{13})\tilde{\tau}(3-\tau_1^3)[K_0(2\tau_1)+\tau_1 K_1(2\tau_1)]$$

$$+\frac{1}{384}(C_{40}+C_{04})[(9-9\tau_1^2+\tau_1^4)K_0(2\tau_1) - 2\tau_1^3 K_1(2\tau_1)] + \cdots \tag{14}$$

where $\tau_1 = (|\,\tilde{\tau}\,|)^{0.5}$, and $K_n(\cdot)$ = modified Bessel function of order n. The coefficients in the above expression are given by the following moments:

$$\int_{-\infty}^{\infty} \tilde{\tau}\, p_{\tilde{\tau}}(\tilde{\tau})\,\mathrm{d}\tilde{\tau} = C_{11} + \frac{11}{8}(C_{31}+C_{13})\,,\quad \int_{-\infty}^{\infty} \tilde{\tau}^2 p_{\tilde{\tau}}(\tilde{\tau})\,\mathrm{d}\tilde{\tau} = 4 + 4(C_{20}+C_{02}) + \frac{25}{4}C_{22}\,,$$

$$\int_{-\infty}^{\infty} \tilde{\tau}^3 p_{\tilde{\tau}}(\tilde{\tau})\,\mathrm{d}\tilde{\tau} = 144C_{11} + 7407(C_{31}+C_{13}) \tag{15}$$

Also, $C_{20} + C_{02} = 0.5(m_{20} + m_{02}) - 2$, and $C_{40} + C_{04} = 24^{-1}(m_{40} + m_{04}) - 1.5(m_{20} + m_{02}) + 4$. Fig. 14 compares the computed $p_{\tilde{\tau}}(\tilde{\tau})$ with those measured closest to the bed (at z = 0.002 m) for Runs 6a and 6b. The values of coefficients are furnished in Table 5. The experimental data collapse satisfactorily on the computed curves, implying adequacy of the derivation of $p_{\tilde{\tau}}(\tilde{\tau})$ using the GC series expansion based on the exponential distribution being applicable to mobile-bed flows.

To analyze the bursting events, the fractional contribution from each event towards the RSS production is given by the random variable $\tilde{\tau} = \langle \tilde{u}\tilde{w} \rangle_{Qi}$ that corresponds to appropriate quadrants. Denoting the PDFs of $Q1$, $Q2$, $Q3$ and $Q4$ events by $p_1(\tilde{\tau})$, $p_2(\tilde{\tau})$, $p_3(\tilde{\tau})$ and $p_4(\tilde{\tau})$, respectively, it follows that

$$p_1(\tilde{\tau}) + p_2(\tilde{\tau}) + p_3(\tilde{\tau}) + p_4(\tilde{\tau}) = p_{\tilde{\tau}}(\tilde{\tau}) \tag{16}$$

It was shown by Bose and Dey (2010) that

$$p_1(\tilde{\tau} > 0) = \frac{1}{2} p_{\tilde{\tau}}(\tilde{\tau}) + \frac{1}{4}(C_{10} - C_{01})\tau_1\, K_1(2\tau_1) - \frac{1}{96}(C_{30} - C_{03})\tau_1[\tau_1\, K_0(2\tau_1) + (4-\tau_1)K_1(2\tau_1)]$$

$$+\frac{1}{32}(C_{21} - C_{12})\tau_1[\tau_1 K_0(2\tau_1) + (1-\tau_1^2)K_1(2\tau_1)] + \cdots \tag{17}$$

$$p_2(\tilde{\tau} < 0) = \frac{1}{2} p_{\tilde{\tau}}(\tilde{\tau}) - \frac{1}{4}(C_{10} - C_{01})\tau_1\, K_1(2\tau_1) + \frac{1}{96}(C_{30} - C_{03})\tau_1\left[\tau_1 K_0(2\tau_1) + (4-\tau_1)K_1(2\tau_1)\right]$$

$$-\frac{1}{32}(C_{21} - C_{12})\tau_1[\tau_1\, K_0(2\tau_1) + (1-\tau_1^2)K_1\tau_1] + \cdots \tag{18}$$

In the above expressions, the coefficient $C_{21} - C_{12}$ is given by

$$\int_{0}^{\infty} \tilde{\tau}\, p_1(\tilde{\tau})\,\mathrm{d}\tilde{\tau} = \frac{1}{2}\int_{0}^{\infty} \tilde{\tau}\, p_{\tilde{\tau}}(\tilde{\tau})\,\mathrm{d}\tilde{\tau} + \frac{1}{4}(C_{10} - C_{01}) - \frac{3}{32}(C_{21} - C_{12}) \tag{19}$$

Figs. 15(a and b) compare the computed $p_i(\tilde{\tau})$ with those measured closest to the bed (at z = 0.002 m) for Runs 6a and 6b. Table 6 provides computed values of coefficients. It is evident that the conditional RSS corresponding to the bursting events can be well represented by the PDFs derived from a GC series expansion based on the exponential distribution being effectively applicable to mobile-bed flows.

10. DISCUSSION

In the preceding sections, we have experimentally identified primarily the near-bed turbulence characteristics corresponding to a bed-load transport. Now, a conceptual framework can be planned to explain the physics of sediment transport. As a remark, we would here like to clarify the link between the findings of the near-bed turbulence characteristics and the visual observation of the sediment motion in mobile-bed flows.

A close observation during the bed-load transport revealed that the sediment entrainment takes place as a common temporal (but continual) motion of many particles from the isolated regions of the bed with changing locations very frequently covering the entire bed surface. This is well-known to be governed by an intermittent coherent structure of turbulence. Grass (1971) and Schmid (1985) postulated that the bed-load transport originates from the sweep events, while they interact with the bed. The sweep events during the sediment transport have been quantified in this study contributing about 70% towards the total RSS production [Figs. 12(a)]. The near-bed shearing flow is highly retarded interacting with the bed roughness developing front vortex (Λ-vortex) that has an intense vorticity core under pressure. Fig. 16 shows the conceptual schematic of the coherent structure during the sediment motion; the sweeps are the part of a Λ-vortex system, as a potential physical process of bed-load transport. In fact, the retardation produces a Λ-vortex capable of dislodging the sediment particles from the bed surface through its low-pressure core and they are drifted by the near-bed flow. Therefore, the most provoking turbulence characteristic towards the bed-load transport is a sweep producing low-pressure field, as confirmed in this study by the drastic change in pressure energy diffusion rate to a negative value (see Fig. 11). It induces a lift force transporting the bed particles collectively from the isolated regions, as was visually observed. The arrival of Λ-vortex system is rather temporal and intermittent, but covers the whole bed surface in succession of arrivals making a continual sediment motion, as a bed-load transport. This concept is, in fact, the basis of the sediment motion by the turbulent flows, but it has not so far been given much attention in modeling the sediment transport.

The results of this study are therefore instrumental in resolving a number of important issues that can address how to analyze the sediment transport phenomenon, as a future scope of research. The most important is how best to incorporate the sweep events into a theoretical model describing the sediment transport process. Thus, the knowledge of how the sweep events to contribute towards the near-bed RSS production governing the sediment motion would be an essential prerequisite. In the near-bed flow zone, a gain in turbulence production due to negative pressure energy diffusion rate is another aspect that can be given adequate importance for developing a theoretical model. As the TKE-production and dissipation rates are almost equal for mobile-bed flow (Fig. 11), little is contributed from the TKE-production rate towards the sediment motion. Also, a reduction in near-bed TKE-dissipation rate leads to an increase in near-bed eddy size, as reflected from the Taylor microscale in mobile-bed flows [Fig. 8(a)]. A modified parameterization for the Basset term (Basset 1888) containing the temporal change of flow velocity relative to that of a particle velocity could also be prepared for inclusion in a model of sediment transport. The potential proposition of the modified turbulent boundary layer characteristics due to sediment motion could be as follows:

Parker *et al.* (2003) put forward a bed-load transport model, where the transport rate was related to an increasing function of the excess of the residual bed shear stress. The residual bed shear stress was obtained from the fluid residual shear stress on the bed in excess of its critical value. The foundation behind the model development was that the residual shear stress could be taken as a measure of the predominating bursting events close to the bed. It therefore characterizes the potentiality of the flow to produce those bursting events which could be the major hydrodynamics related to the sediment transport. However, Parker *et al.* (2003) assumed a linear variation of the average particle transport rate with the excess of the residual bed shear stress owing to dearth of detailed experimental observations. Therefore, the present experimental findings would be prompted in investigating the correlation between the residual fluid shear stress on the bed and the bursting events in the shear boundary layer. Further, the overall transfer of momentum from the fluid to the solid phase and the residual fluid shear stress on the bed could be calculated employing the results of this study. It has been already indicated the disadvantage in calculating the fluid bed shear stress from the bed slope balancing the gravity in presence of bed-load transport. These results therefore allow (i) to carefully elaborate a more accurate parameterization for the reduction of RSS in presence of bed-load transport and (ii) to define a relationship between the average bed-load transport rate and the residual bed shear stress. Regarding the log-law of wall in mobile-bed flows, the application of traditional log-law is highly questionable due to reduced value of von Kármán coefficient (leading to a reduced the traversing length of an eddy) and elevated levels of virtual bed and zero-velocity. Last but not the least, as the near-bed turbulence creates the sediment transport process highly probabilistic, the universal PDF distributions for the turbulence parameters developed by Bose and Dey (2010) could be employed in developing a more realistic model for bed-load transport. It can be concluded that the state-of-the-art of the bed-load transport models including local turbulence properties of fluid-particle interactions is in an embryonic state. Further research is therefore required for mobile-bed flows preferably by using high resolution flow measuring and visualizing techniques to characterize these findings in the context of bed-load transport.

11. CONCLUSIONS

In this study, experiments were carried out to measure the turbulence characteristics in clear-water and mobile-bed flows by a *Vectrino* probe. Analysis of experimental data has allowed revealing the modifications in the turbulence parameters due to the difference in bed conditions. As the influence of bed-load transport on the turbulence has been the main focus, the experimental results for clear-water flows have been used as reference. For a lucid comprehension, the predominating turbulence parameters in the inner- and outer-region of for clear-water and mobile-bed flows are schematically displayed in Figs. 17(a – d). The important conclusions related to the influence of bed-load transport on the turbulence characteristics are as follows:

A reduction in RSS distributions over the entire flow depth in presence of bed-load transport is associated with the provided momentum from the main flow to maintain sediment particle motion overcoming the bed resistance. The near-bed RSS distributions undergo an excessive damping due to a diminishing level of turbulence fluctuations resulting from a fall in magnitude of flow velocity relative to particle velocity transporting sediment particles [Fig. 17(a)]. It leads to a reduction of mobile-bed flow resistance and friction factor. The log-law in presence of bed-load transport is characterized by a decrease in von Kármán coefficient and an increase in levels of the virtual bed and the zero-velocity. The traversing length of an eddy decreases, but the eddy size increases in mobile-bed flows, as compared to those in clear-water flows. The analysis of third-order correlations reveals that during the bed-load transport, a streamwise acceleration directing downward is established and associated with a streamwise diffusion of vertical RNS and a downward diffusion of streamwise RNS [Fig. 17(b)]. In the near-bed flow zone, the bed-load transport is associated with a positive streamwise TKE-flux directing towards the flow and a negative vertical TKE-flux directing downward [Fig. 17(c)]. The influence of bed-load transport on the TKE-budget is pronounced, reducing the TKE-production rate and changing the pressure energy diffusion rate drastically to negative magnitude in the near-bed flow zone [Fig. 17(c)]. Conditional statistics of RSS suggests that the sweep events are the prevailing mechanism towards the bed-load transport [Fig. 17(d)]. The PDF distributions of turbulence parameters close to the bed for mobile-bed flows could be adequately predicted by the universal PDFs developed by Bose and Dey (2010) using a GC series expansion based on the exponential distribution.

References

Balachandra, R., and F. Bhuiyan (2007), Higher-order moments of velocity fluctuations in an open-channel flow with large bottom roughness, *J. Hydraul. Eng.* **133** (1), 77-87.

Basset, A.B. (1888), *A Treatise on Hydrodynamics*, Cambridge University Press, U.K.

Bennet, S.J., and J.S. Bridge (1995), An experimental study of flow, bedload transport and bed topography under conditions of erosion and deposition and comparison with theoretical models, *Sedimentology* **42** (1), 117-146.

Bennett, S.J., J.S. Bridge, and J.L. Best (1998), Fluid and sediment dynamics of upper stage plane beds, *J. Geophys. Res.* **103** (C1), 1239-1274.

Bergeron, N.E., and P. Carbonneau (1999), The effect of sediment concentration on bedload roughness, *Hydrol. Process.* **13** (16), 2583-2589.

Best, J. (1992), On the entrainment of sediment and initiation of bed defects: insights from recent developments within turbulent boundary layer research, *Sedimentology* **39**, 797-811.

Best, J., S. Bennett, J. Bridge, and M. Leeder (1997), Turbulence modulation and particle velocities over flat sand beds at low transport rates, *J. Hydraul. Eng.* **123** (12), 1118-1129.

Blanckaert, K., and U. Lemmin (2006), Means of noise reduction in acoustic turbulence measurements, *J. Hydraul. Res.* **44** (1), 1-17.

Bose, S.K., and S. Dey (2010), Universal probability distributions of turbulence in open channel flows, *J. Hydraul. Res.* **48** (3), 388-394.

Calomino, F., R. Gaudio, and A. Miglio (2004), Effect of bed-load concentration on friction factor in narrow channels, *Proc. Second Int. Conf. Fluvial Hydraul.*, *River Flow 2004*, Volume 1, Taylor and Francis, London, U.K., 279-285.

Campbell, L., I. McEwan, V. Nikora, D. Pokrajac, M. Gallagher, and C. Manes (2005), Bed-load effects on hydrodynamics of rough-bed open-channel flows, *J. Hydraul. Eng.* **131** (7), 576-585.

Carbonneau, P.E., and N.E. Bergeron (2000), The effect of bedload transport on mean and turbulent flow properties, *Geomorphology* **35**, 267-278.

Clifford, N.J., J. McClatchey, and J.R. French (1991), Measurements of turbulence in the benthic boundary layer over a gravel bed and comparison between acoustic measurements and predictions of the bedload transport of marine gravels, *Sedimentology* **38**, 161-171.

Crowe, C.T. (1993), Modelling turbulence in multiphase flows, *Engineering Turbulence Modelling and Experiments*, Volume 2, W. Rodi, and F. Martelli, eds., Elsevier, Amsterdam, The Netherlands, 899-913.

Detert, M., V. Weitbrecht, and G.H. Jinka (2010), Laboratory measurements on turbulent pressure fluctuations in and above gravel beds, *J. Hydraul. Eng*. **136** (10), 779-789.

Dey, S., and R.V. Raikar (2007), Characteristics of loose rough boundary streams at near-threshold, *J. Hydraul. Eng*. **133** (3), 288-304.

Dey, S., S. Sarkar, and L. Solari (2011), Near-bed turbulence characteristics at the entrainment threshold of sediment beds, *J. Hydraul. Eng.* **137** in press.

Drake, T.G., R.L. Shreve, W.E. Dietrich, P.J. Whiting, and L.B. Leopold (1988), Bedload transport of fine gravel observed by motion picture photography, *J. Fluid Mech.* **192**, 193-217.

Gallagher, M., I. McEwan, and V. Nikora (1999), The changing structure of turbulence over a self-stabilising sediment bed, *Internal Rep. No. 21*, Department of Engineering, University of Aberdeen, Aberdeen, U.K.

Gaudio, R., A. Miglio, and F. Calomino (2011), Friction factor and von Karman's κ in open channels with bed-load. *J. Hydraul. Res.* **49** (2), 245-253.

Gaudio, R., A. Miglio, and S. Dey (2010), Nonuniversality of von Kármán's κ in fluvial streams. *J. Hydraul. Res.* **48** (5), 658-663.

Gore, R.A., and C.T. Crowe (1991), Modulation of turbulence by a dispersed phase, *J. Fluids Eng.* **113** (6), 304-307.

Goring, D.G., and V.I. Nikora (2002), Despiking acoustic Doppler velocimeter data, *J. Hydraul. Eng.* **128** (1), 117-126.

Grass, A.J. (1970), Initial instability of fine bed sand, *J. Hydraul. Div.* **96** (3), 619-632.

Grass, A.J. (1971), Structural features of turbulent flow over smooth and rough boundaries, *J. Fluid Mech.* **50**, 233-255.

Gust, G., and J.B. Southard (1983), Effects of weak bed load on the universal law of the wall, *J. Geophys. Res*. **88** (C10), 5939-5952.

Gyr, A., and A. Schmid (1997), Turbulent flows over smooth erodible sand beds in flumes, *J. Hydraul. Res.* **35** (4), 525-544.

Heathershaw, A.D., and P.D. Thorne (1985), Sea-bed noises reveal role of turbulent bursting phenomenon in sediment transport by tidal currents, *Nature* **316**, 339-342.

Hetsroni, G. (1993), The effect of particles on the turbulence in a boundary layer, *Particulate Two-Phase Flow*, M.C. Raco, ed., Butterworth-Heinemann, 244-264.

Kline, S.J., W.C. Reynolds, F.A. Schraub, and P.W. Runstadler (1967), The structure of turbulent boundary layers, *J. Fluid Mech.* **30**, 741-773.

Krogstad, P.Å., R.A. Antonia, and L.W.B. Browne (1992), Comparison between rough- and smooth-wall turbulent boundary layers, *J. Fluid Mech.* **245**, 599-617.

Lacey, R.W.J., and A.G. Roy (2008), Fine-scale characterization of the turbulent shear layer of an instream pebble cluster. *J. Hydraul. Eng*. **134** (7), 925-936.

Lu, S.S., and W.W. Willmarth (1973), Measurements of the structures of the Reynolds stress in a turbulent boundary layer, *J. Fluid Mech.* **60**, 481-511.

Monin, A.S., and A.M. Yaglom (2007), *Statistical Fluid Mechanics, Volume II: Mechanics of Turbulence*, Dover Publications, New York, USA.

Nakagawa, H., and I. Nezu (1977), Prediction of the contributions to the Reynolds stress from bursting events in open-channel flows, *J. Fluid Mech*. **80**, 99-128.

Nelson, J.M., R.L. Shreve, S.R. McLean, and T.G. Drake (1995), Role of near-bed turbulence structure in bed load transport and bed form mechanics, *Wat. Resour. Res.* **31** (8), 2071-2086.

Nezu, I., and H. Nakagawa (1993), *Turbulence in Open-Channel Flows*, Balkema, Rotterdam, Netherlands.

Nikora, V.I., and D.G. Goring (1999), Effects of bed mobility on turbulence structure, *NIWA Internal Rep. No. 48*, National Institute of Water and Atmospheric Research, Christchurch, New Zealand.

Nikora, V., and D. Goring (2000), Flow turbulence over fixed and weakly mobile gravel beds, *J. Hydraul. Eng*. **112** (5), 335-355.

Nikora, V., D. Goring, I. McEwan, and G. Griffiths (2001), Spatially averaged open-channel flow over rough bed, *J. Hydraulic Eng.* **127** (2), 123-133.

Owen, P.R. (1964), Saltation of uniform grains in air, *J. Fluid Mech*. **20**, 225-242.

Papanicolaou, A.N., P. Diplas, C. Dancey, and M. Balakrishnan (2001), Surface roughness effects in near-bed turbulence: implications to sediment entrainment, *J. Eng. Mech.* **127** (3), 211-218.

Parker, G., G. Seminara, and L. Solari (2003), Bedload at low Shields stress on arbitrarily sloping beds: Alternative entrainment formulation, *Wat. Resour. Res.* **39**, 1249, doi:10.1029/2001WR000681.

Pitlick, J. (1992), Flow resistance under conditions of intense gravel transport, *Wat. Resour. Res.* **28**, 891-903.

Pope, S.B. (2001), *Turbulent Flows*, Cambridge University Press, U.K.

Radice, A., and F. Ballio (2008), Double-average characteristics of sediment motion in one-dimensional bed load, *Acta Geophys*. **56** (3), 654-668.

Raupach, M.R. (1981), Conditional statistics of Reynolds stress in rough-wall and smooth-wall turbulent boundary layers, *J. Fluid Mech.* **108**, 363-382.

Robinson, S.K. (1991), The kinematics of turbulent boundary layer structure, *NASA TM-103859*.

Sarkar, S., and S. Dey (2010), Double-averaging turbulence characteristics in flows over a gravel-bed, *J. Hydraul. Res*. **48** (6), 801-809.

Schmid, A. (1985), Wandnahe turbulente bewegungsabläufe und ihre bedeutung für die riffelbildung, Ph.D. thesis and *Report R22-85*, Institute for Hydromechanics and Water Resources Management, ETH Zürich, Switzerland.

Smith, J.D., and S.R. McLean (1977), Spatially averaged flow over a wavy surface, *J. Geophys. Res.: Oceans* **82** (12), 1735-1746.

Song, T., Y.-M. Chiew, and C.O. Chin (1998), Effect of bed-load movement on flow friction factor, *J. Hydraul. Eng*. **124** (2), 165-175.

Song, T., W.H. Graf, and U. Lemmin (1994), Uniform flow in open channels with movable gravel bed, *J. Hydr. Res.* **32** (6), 861-876.

Sumer, B.M., L.H.C. Chua, N.-S. Cheng, and J. Fredsoe (2003), Influence of turbulence on bed load sediment transport, *J. Hydraul. Eng.* **129** (8), 585-596.

van Rijn, L.C. (1984), Sediment transport, part I: bed-load transport, *J. Hydraul. Eng.* **110** (10), 1431-1456.

Wang, Z., and P. Larsen (1994), Turbulent structure of water and clay suspensions with bed load, *J. Hydraul. Eng.* **120** (5), 577-600.

Yang, Y., and M. Hirano (1995), Discussion on 'Uniform flow in open-channel with movable gravel bed' by T. Song, W.H. Graf, and U. Lemmin, *J. Hydr. Res*. **33** (6), 877-879.

Yang, S.Q., S.K Tan, and S.Y. Lim (2004), Velocity distribution and dip-phenomenon in smooth uniform open channel flows, *J. Hydraul. Eng.* **130** (12), 1179-118.

Yeganeh-Bakhtiary, A., H. Gotoh, and T. Sakai (2000), Applicability of the Euler-Lagrange coupling multiphase-flow model to bed-load transport under high bottom shear, *J. Hydraul. Res.* **38** (5), 389-398.

Yeganeh-Bakhtiary, A., B. Shabani, H. Gotoh, and S.S.Y. Wang (2009), A three-dimensional distinct element model for bed-load transport, *J. Hydraul. Res.* **47** (2), 203-212.

Table 1

Characteristics of sediment used in the experiments: d_{50} is the median diameter of sediments, s is the relative density of sediments, σ_g is the geometric standard deviation of particle size distribution, u_{*c} is the critical shear velocity for the initiation of sediment motion, and ϕ is the angle of repose of sediments.

d_{50} [mm]	s	σ_g	u_{*c} [m/s]	ϕ [deg]
0.95	2.65	1.28	0.0224	27
2.6	2.65	1.20	0.0429	30
4.1	2.65	1.13	0.0575	33

Note: The values of u_{*c} were determined from the Shields diagram.

Table 2

Uncertainty estimation for *Vectrino* data.

d_{50} (mm)	Case	$\overline{u}$ (m/s)	$\overline{v}$ (m/s)	$\overline{w}$ (m/s)	$(\overline{u'u'})^{0.5}$ (m/s)	$(\overline{v'v'})^{0.5}$ (m/s)	$(\overline{w'w'})^{0.5}$ (m/s)	$-\overline{u'w'}$ (m^2/s^2)
0.95	Clear-water	4.32×10^{-3}* (±3.61†)	2.95×10^{-3} (±2.11)	3.67×10^{-3} (±4.89)	5.32×10^{-3} (±4.83)	4.54×10^{-3} (±4.75)	1.98×10^{-3} (±4.92)	7.81×10^{-5} (±8.19)
	Mobile-bed	4.93×10^{-3} (±4.67)	3.29×10^{-3} (±3.09)	2.59×10^{-3} (±4.19)	4.88×10^{-3} (±4.26)	4.56×10^{-3} (±5.01)	5.31×10^{-3} (±3.06)	9.83×10^{-5} (±4.17)
4.1	Clear-water	3.11×10^{-3} (±4.21)	1.83×10^{-3} (±2.25)	3.77×10^{-3} (±4.01)	3.12×10^{-3} (±4.83)	3.66×10^{-3} (±4.19)	4.17×10^{-3} (±4.21)	6.12×10^{-5} (±5.24)
	Mobile-bed	5.23×10^{-3} (±4.03)	4.02×10^{-3} (±4.12)	3.89×10^{-3} (±4.44)	3.8×10^{-3} (±3.32)	2.93×10^{-3} (±3.99)	5.11×10^{-3} (±5.45)	8.38×10^{-5} (±6.74)

*Standard deviation.

†Average of maximum (negative and positive) percentage error.

Table 3

Experimental data: U is the mean velocity, h is the flow depth, S_h is the relative submergence, R is the flow Reynolds number, F is the flow Froude number, g_s is the bed-load transport rate per unit width, u_{*s} is the shear velocity obtained from slope, λ_s is the friction factor obtained from $8(u_{*s}/U)^2$, $u_{*\tau}$ is the shear velocity obtained from RSS, λ_τ is the friction factor obtained from $8(u_{*\tau}/U)^2$, R_* is the particle shear Reynolds number, κ is the von Kármán coefficient, Δz^+ is the nondimensional depth of virtual bed level, ζ^+ is the nondimensional depth of zero-velocity level, ε is the Nikuradse equivalent sand roughness, and S is the streamwise bed slope.

Run	U [m/s]	h [m]	S_h [$\times 10^3$]	R [$\times 10^{-5}$]	F	g_s [kg/(ms)]	u_{*s} [m/s]	λ_s	$u_{*\tau}$† [m/s]	λ_τ	R_*	κ	Δz^+	ζ^+	ε [mm]
d_{50} = 0.95 mm; S = 0.13%															
1a	0.594	0.10	9.5	2.4	0.60	–	0.036	0.029	0.036	0.030	69	0.40	0.45	0.039	1.11
1b	0.594	0.10	9.5	2.4	0.60	2×10^{-3}	0.036	0.029	0.033	0.025	63	0.37	0.20	0.045	1.28
2a	0.628	0.12	7.9	3.0	0.58	–	0.039	0.031	0.037	0.029	70	0.42	0.41	0.033	0.94
2b	0.628	0.12	7.9	3.0	0.58	3.5×10^{-3}	0.039	0.031	0.036	0.027	69	0.39	0.30	0.039	1.11
3a	0.665	0.15	6.3	4.0	0.55	–	0.044	0.035	0.039	0.028	75	0.41	0.50	0.035	1.00
3b	0.665	0.15	6.3	4.0	0.55	7×10^{-3}	0.044	0.035	0.037	0.025	71	0.39	0.12	0.047	1.34
d_{50} = 2.6 mm; S = 0.30%															
4a	0.767	0.10	26.0	3.1	0.77	–	0.054	0.040	0.057	0.043	294	0.41	0.32	0.03	2.34
4b	0.767	0.10	26.0	3.1	0.77	2×10^{-3}	0.054	0.040	0.051	0.035	265	0.38	0.36	0.032	2.50
5a	0.813	0.12	21.7	3.9	0.75	–	0.059	0.043	0.057	0.040	299	0.41	0.55	0.039	3.04
5b	0.813	0.12	21.7	3.9	0.75	3.5×10^{-3}	0.059	0.043	0.052	0.033	270	0.38	0.18	0.038	2.96
6a*	0.851	0.15	17.3	5.1	0.70	–	0.066	0.049	0.059	0.039	308	0.42	0.35	0.031	2.42
6b*	0.851	0.15	17.3	5.1	0.70	7×10^{-3}	0.066	0.049	0.053	0.031	277	0.37	0.21	0.048	3.74
d_{50} = 4.1 mm; S = 0.38%															
7a	0.839	0.12	34.2	4.0	0.77	–	0.067	0.051	0.065	0.048	533	0.42	0.3	0.023	2.83
7b	0.839	0.12	34.2	4.0	0.77	3.5×10^{-3}	0.067	0.051	0.059	0.040	485	0.35	0.17	0.039	4.80
8a	0.918	0.15	27.3	5.5	0.76	–	0.075	0.053	0.067	0.043	549	0.41	0.27	0.039	4.80
8b	0.918	0.15	27.3	5.5	0.76	7×10^{-3}	0.075	0.053	0.062	0.037	508	0.35	0.16	0.033	4.06

*Runs used for length-scales and higher-order correlations analyses.

†The values of shear velocity used for analysis.

Table 4

Coefficients and skewness for the computation of $p_{\tilde{u}}(\tilde{u})$ and $p_{\tilde{w}}(\tilde{w})$.

Case	C_{10}	C_{01}	C_{20}	C_{02}	C_{30}	C_{03}	C_{40}	C_{04}	M_{30}	M_{03}
Clear-water	0.0139	–0.0080	–0.5435	–0.5179	–0.0309	0.0224	0.7430	0.6908	–0.0650	0.0650
Mobile-bed	–0.0011	–0.0039	–0.5137	–0.5141	0.0081	0.0014	0.6505	0.6687	0.0400	–0.0460

Table 5

Coefficients for the computation of $p_{\tilde{\tau}}(\tilde{\tau})$.

Case	C_{11}	$C_{20} + C_{02}$	$C_{31} + C_{13}$	$C_{40} + C_{04}$
Clear-water	–0.29070	–1.06142	0.00043	1.43360
Mobile-bed	–0.33452	–0.57970	0.37817	0.97779

Table 6

Coefficients for the computation of $p_i(\tilde{\tau})$.

Case	$C_{10} – C_{11}$	$C_{30} – C_{03}$	$C_{21} – C_{12}$
		$p_1(\tilde{\tau})$	
Clear-water	0.02192	–0.07417	–1.3076
Mobile-bed	0.00279	0.00288	–1.3730
		$p_2(\tilde{\tau})$	
Clear-water	0.02192	-0.07417	1.1682
Mobile-bed	0.00279	0.00288	1.0670
		$p_3(\tilde{\tau})$	
Clear-water	0.02192	–0.07417	–1.0738
Mobile-bed	0.00279	0.00288	–1.0922
		$p_4(\tilde{\tau})$	
Clear-water	0.02192	–0.07417	1.0668
Mobile-bed	0.00279	0.00288	1.2036

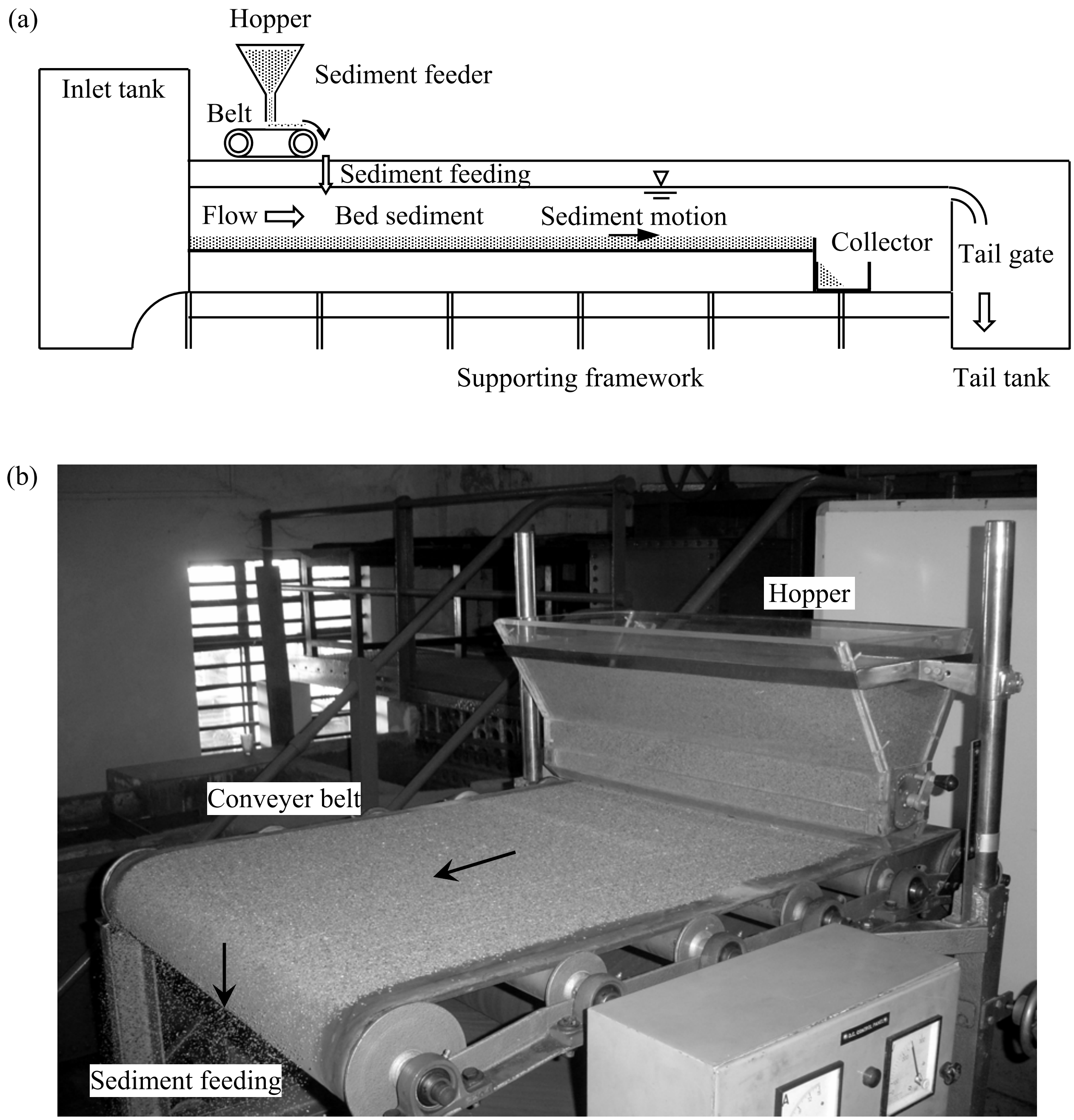

Fig. 1. (a) Schematic of experimental setup and (b) photograph of sediment feeding arrangement. Direction of the sediment feeding is different from that shown in schematic due to the photographic angle.

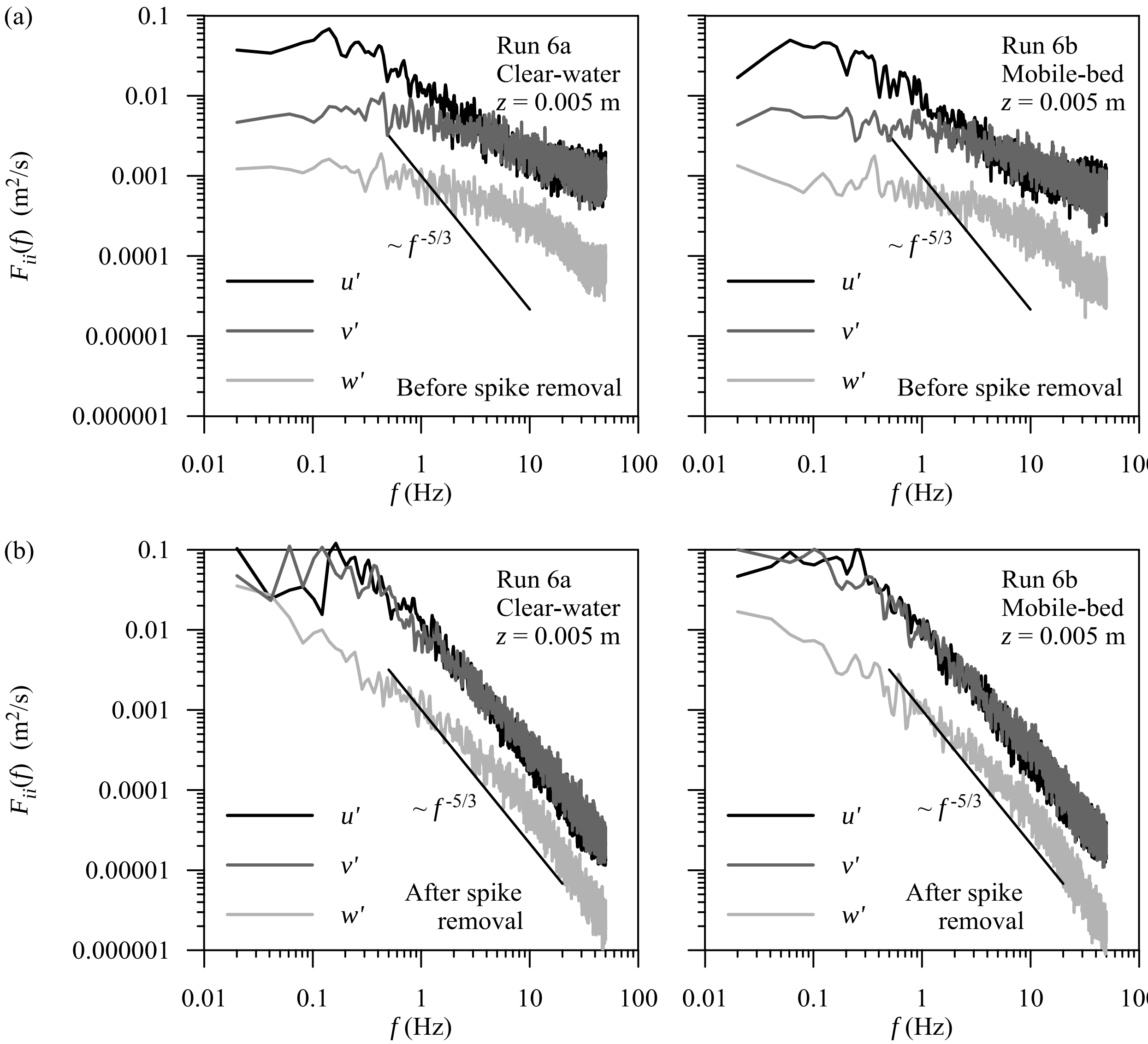

Fig. 2. Velocity power spectra $F_{ii}(f)$ for clear-water and mobile-bed cases: (a) before spike removal and (b) after spike removal.

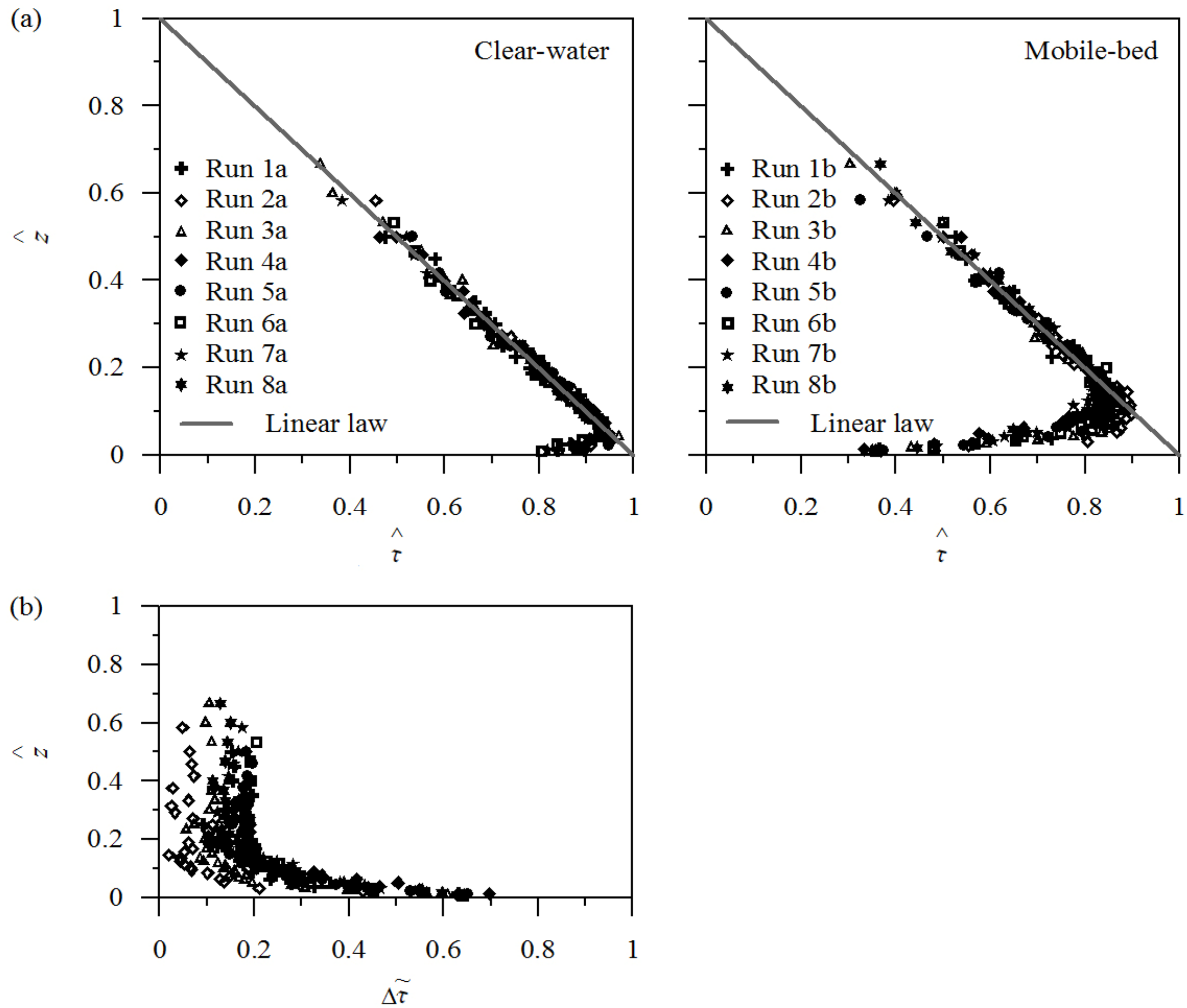

Fig. 3. Vertical distributions of (a) nondimensional RSS $\hat{\tau}$ for clear-water and mobile-bed cases and (b) relative difference of RSS $\Delta\tilde{\tau}$ between clear-water and mobile-bed cases.

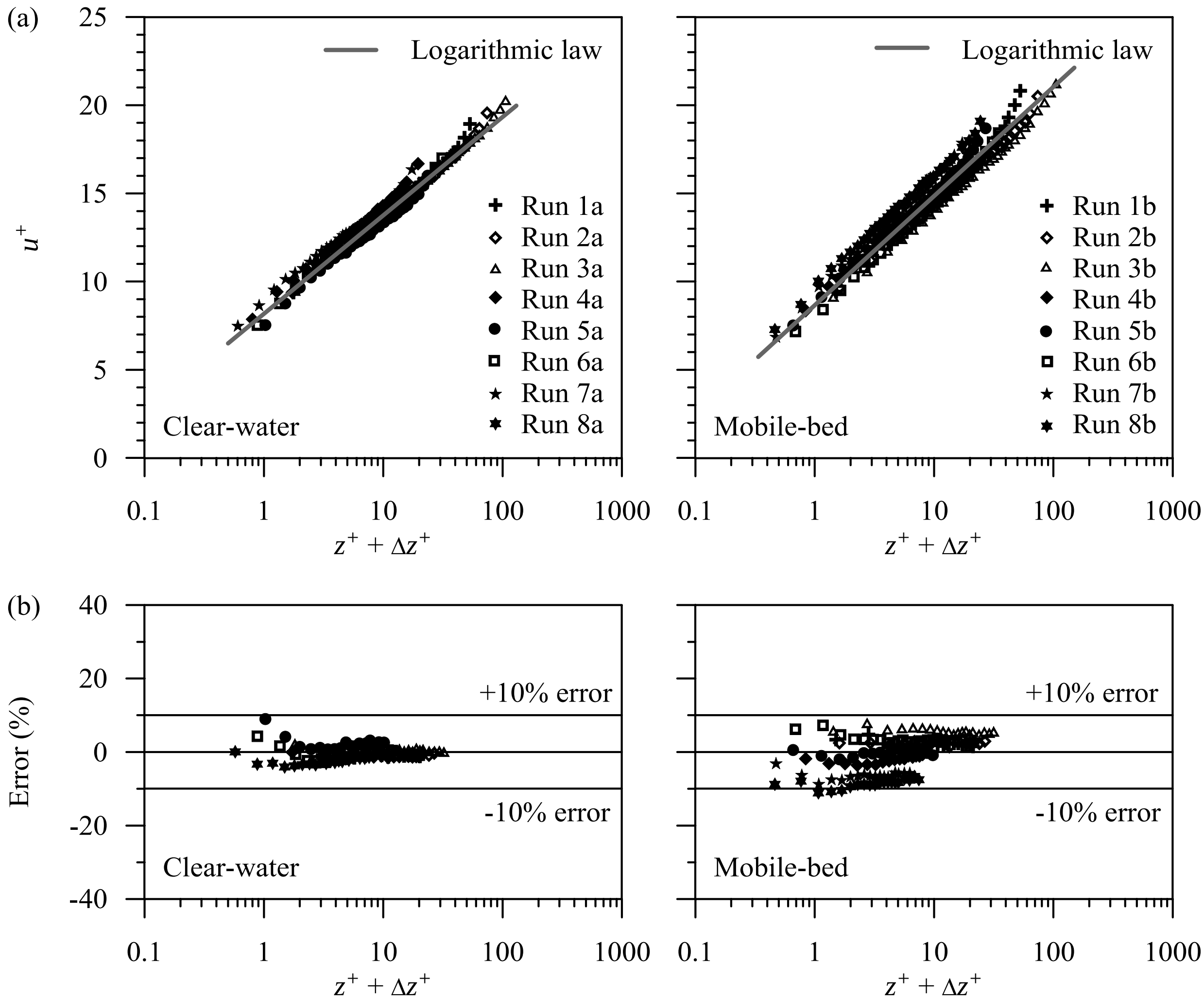

Fig. 4. Vertical distributions of (a) nondimensional time-averaged streamwise velocity u^+ and (b) error in prediction of u^+ from the log-law for clear-water and mobile-bed cases.

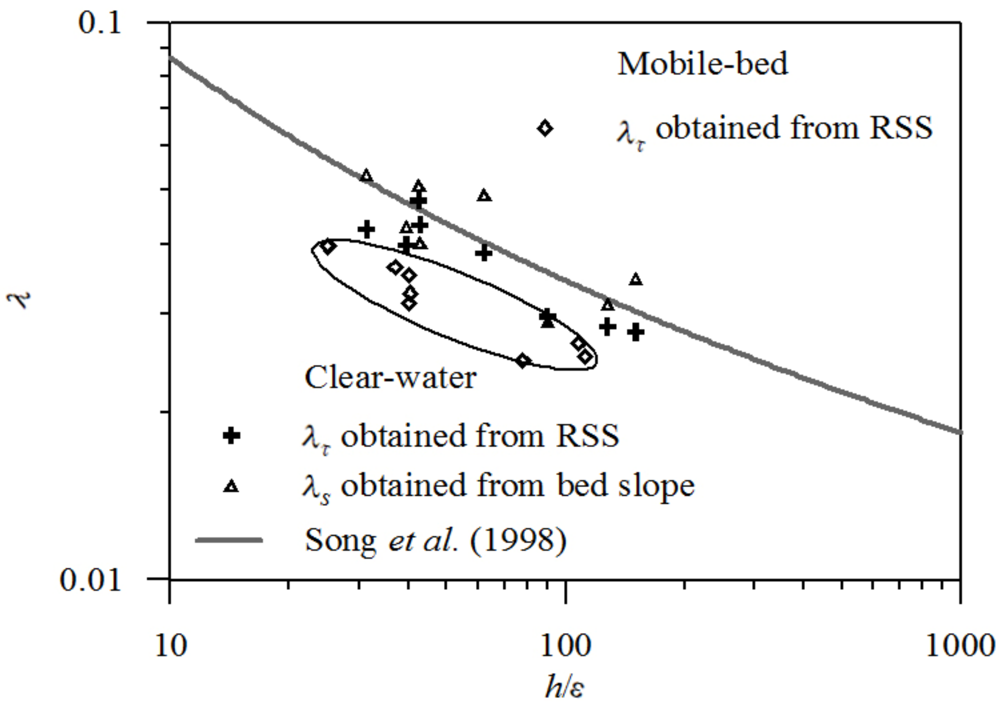

Fig. 5. Friction factor λ dependency on h/ε for clear-water and mobile-bed cases.

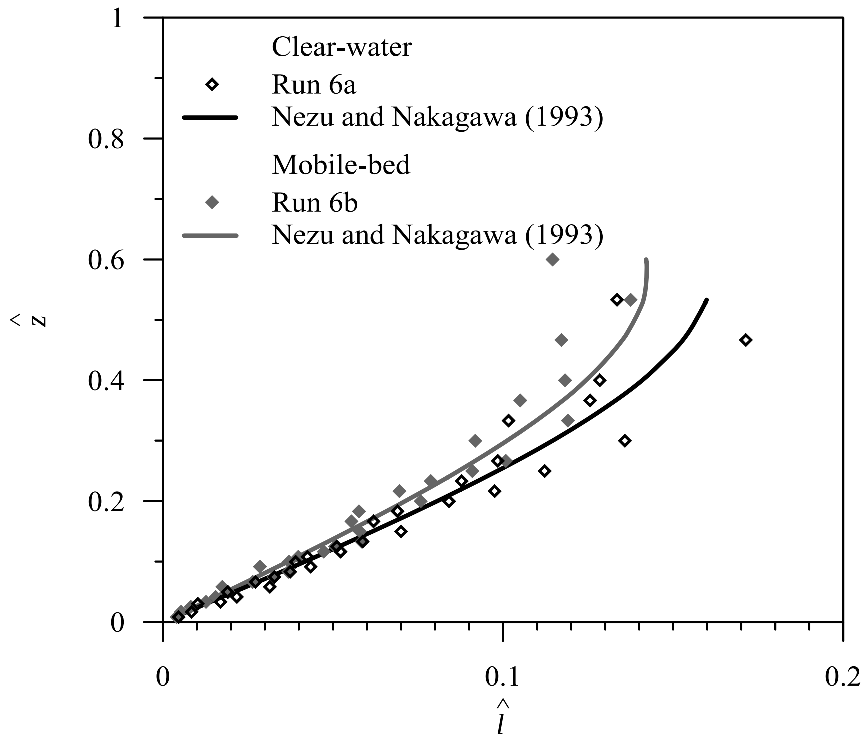

Fig. 6. Mixing length $\hat{l}$ as a function of flow depth for clear-water and mobile-bed cases.

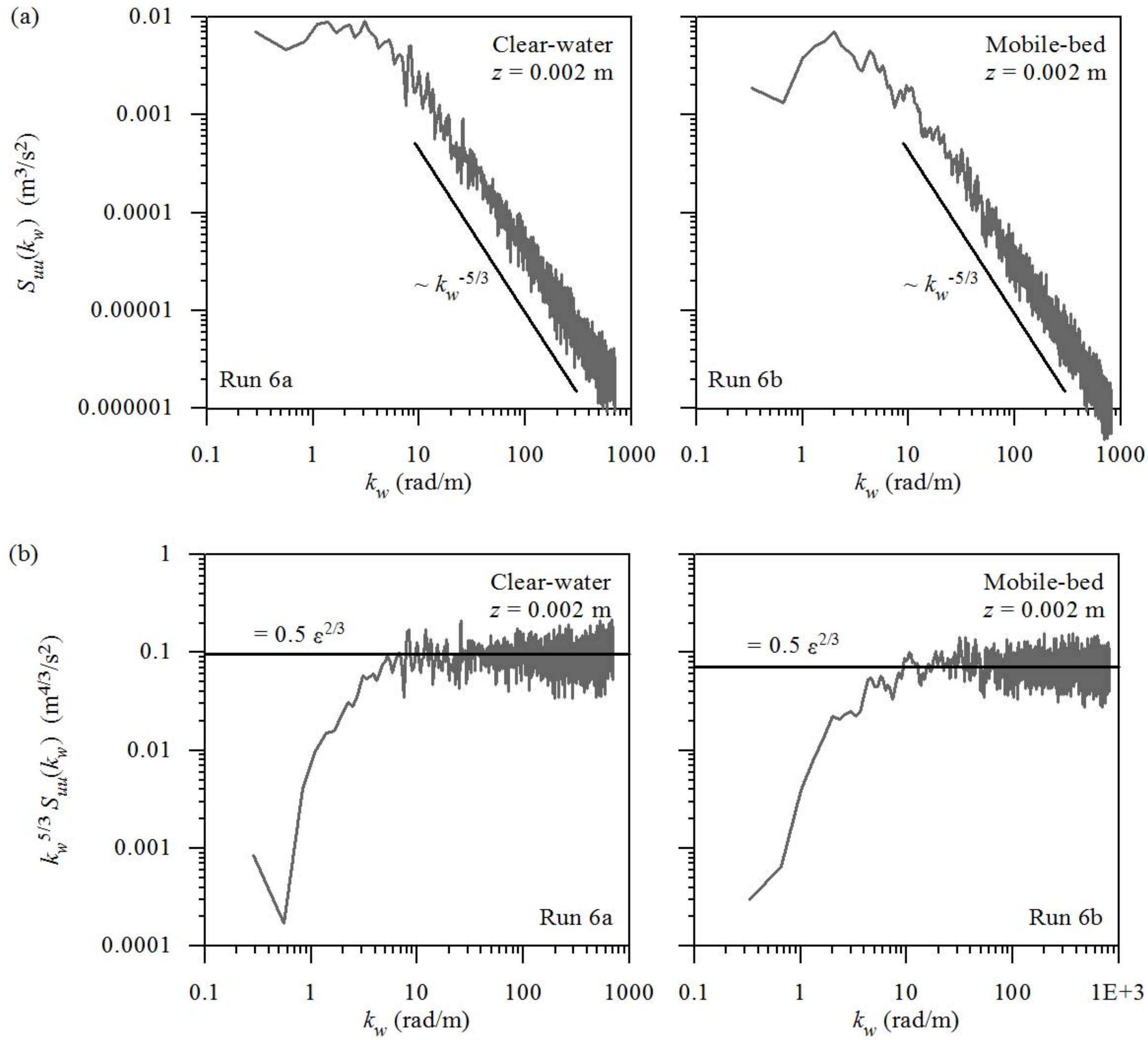

Fig. 7. (a) Velocity power spectra $S_{uu}(k_w)$ and (b) estimation of turbulent dissipation rate ε for clear-water and mobile-bed cases.

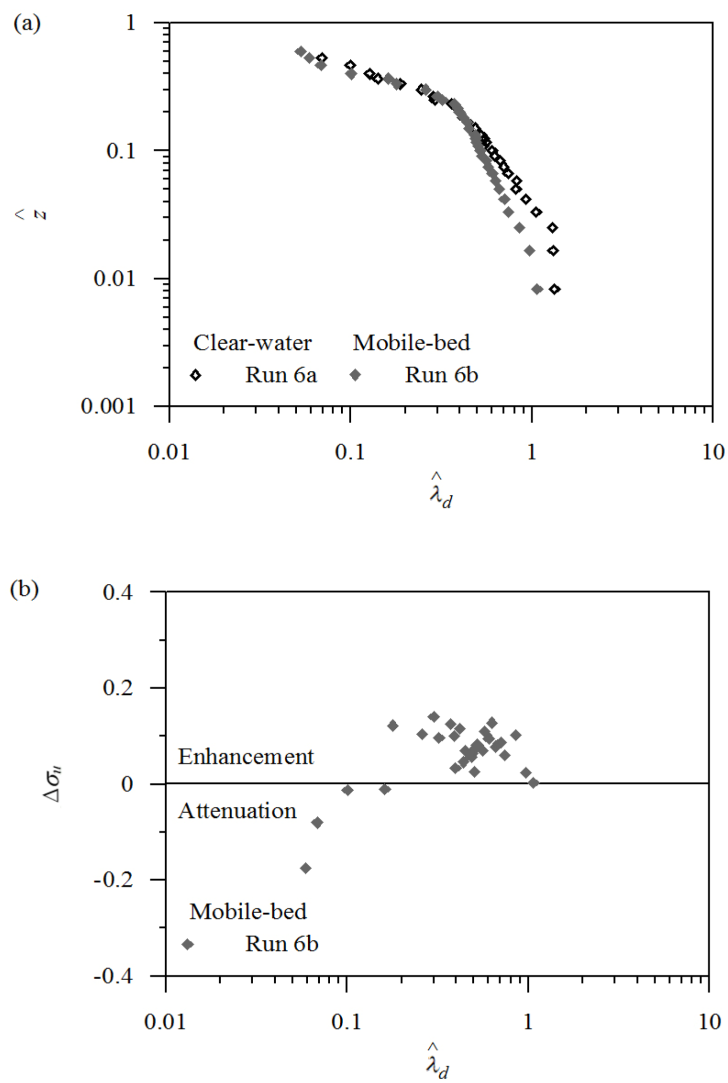

Fig. 8. (a) Ratio of particle size to Taylor microscale $\hat{\lambda}_d$ as a function of flow depth for clear-water and mobile-bed cases and (b) $\hat{\lambda}_d$ for mobile-bed flows as a function of relative difference of streamwise turbulence intensities $\Delta\sigma_u$ between clear-water and mobile-bed cases.

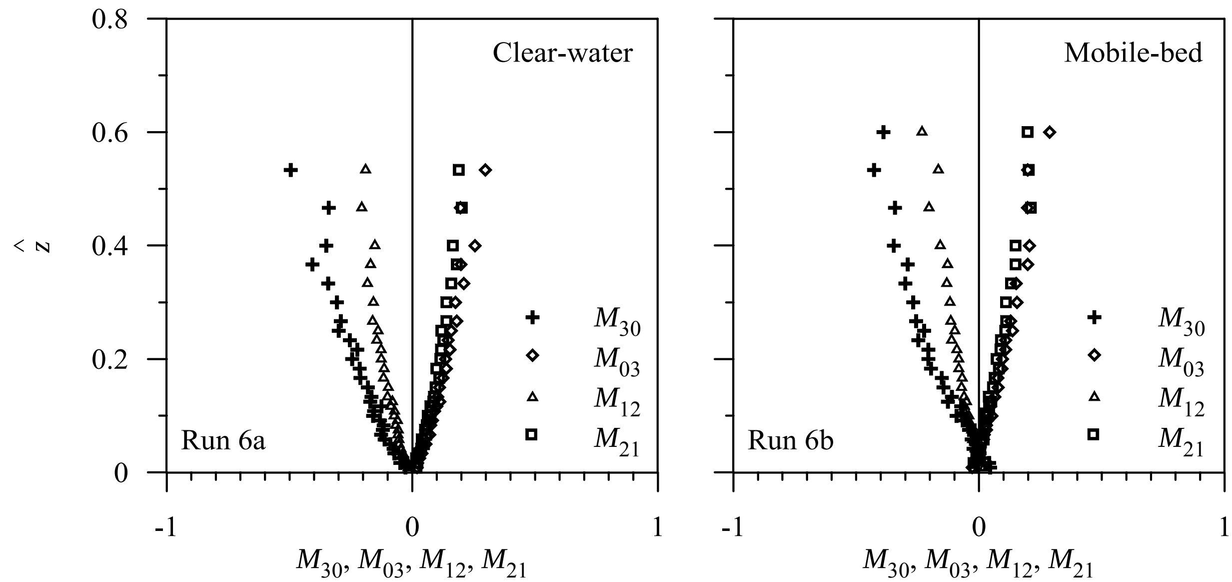

Fig. 9. Vertical distributions of third-order correlations M_{jk} for clear-water and mobile-bed cases.

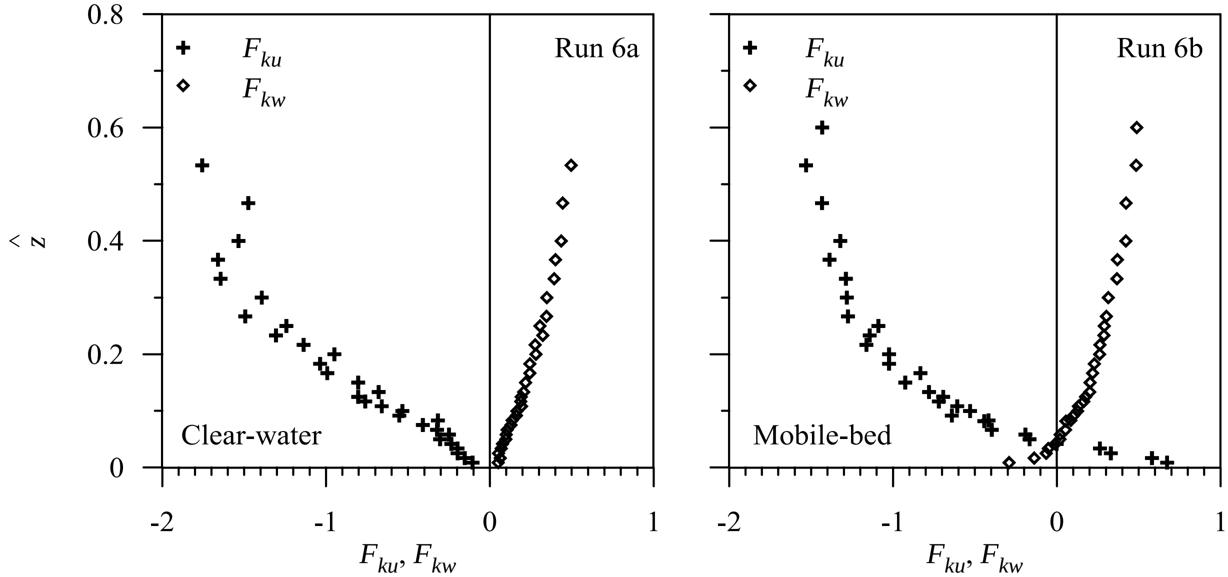

Fig. 10. Vertical distributions of TKE-flux components F_{ku} and F_{kw} for clear-water and mobile-bed cases.

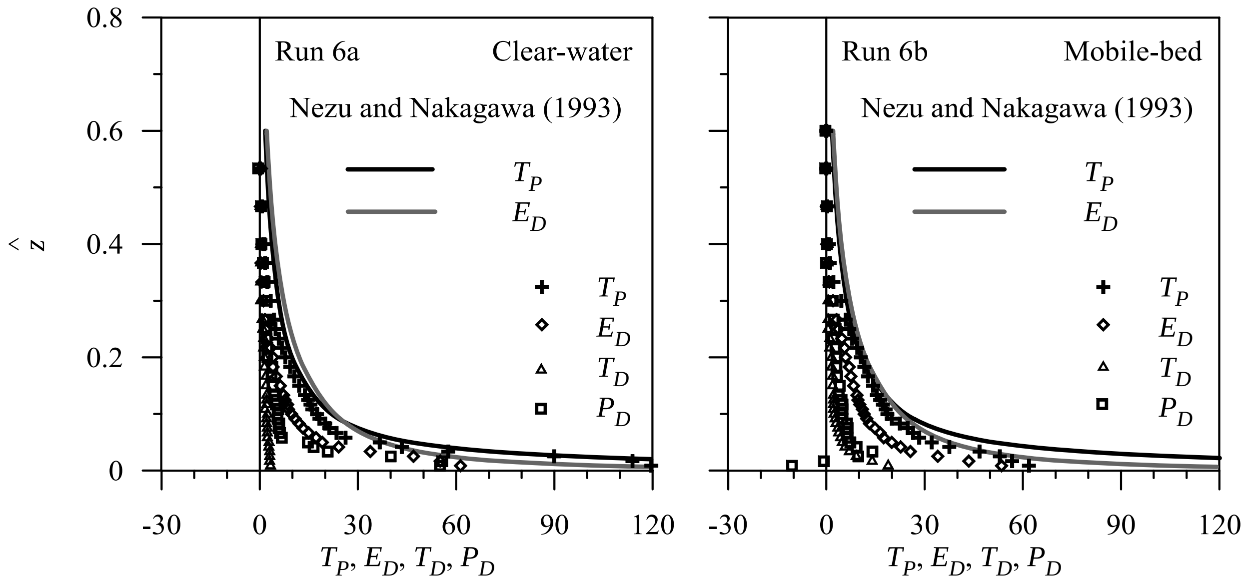

Fig. 11. Vertical distributions of TKE-budgets for clear-water and mobile-bed cases.

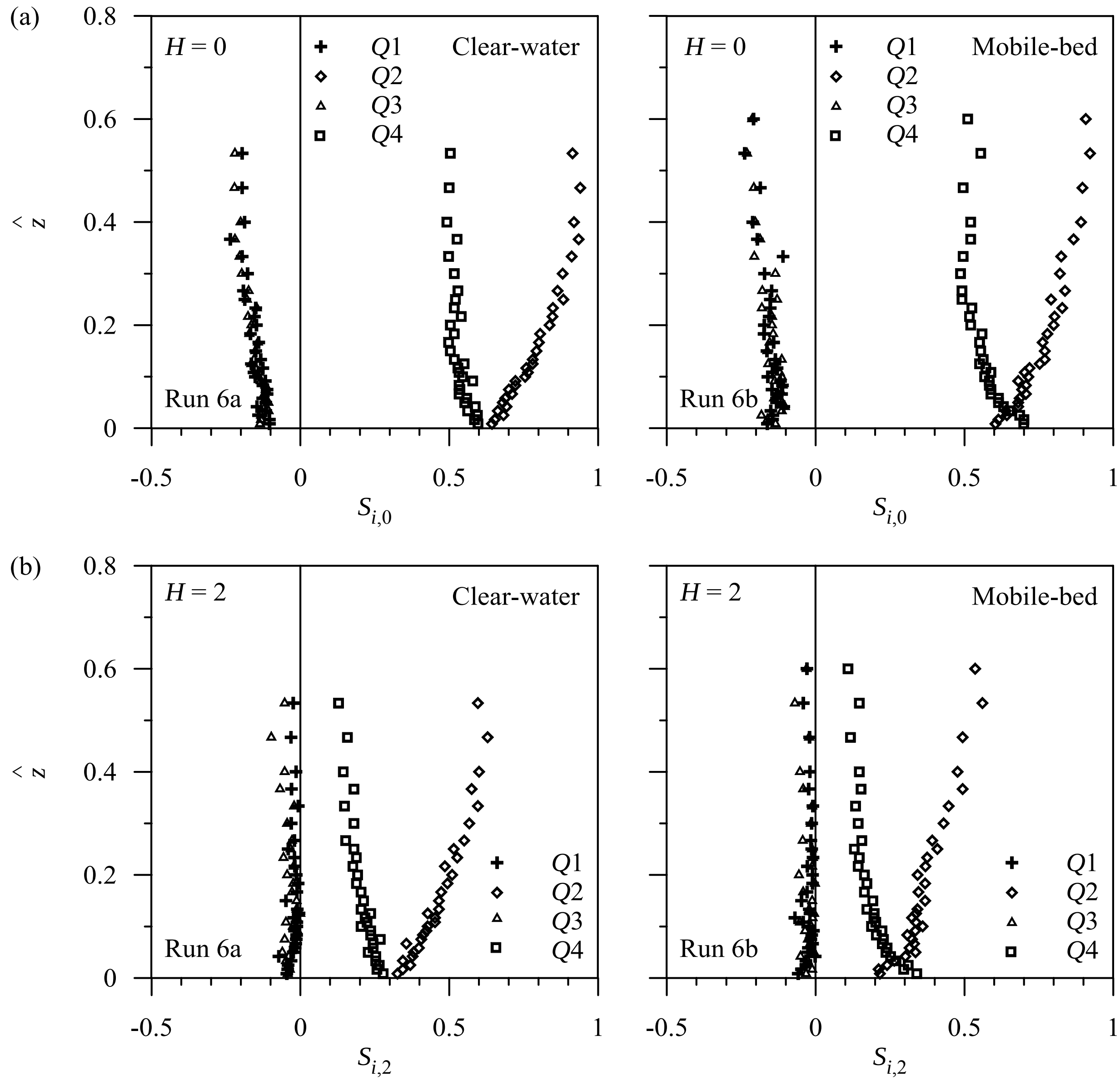

Fig. 12. Vertical distributions of (a) $S_{i,0}(\hat{z})$ and (b) $S_{i,2}(\hat{z})$ for clear-water and mobile-bed cases.

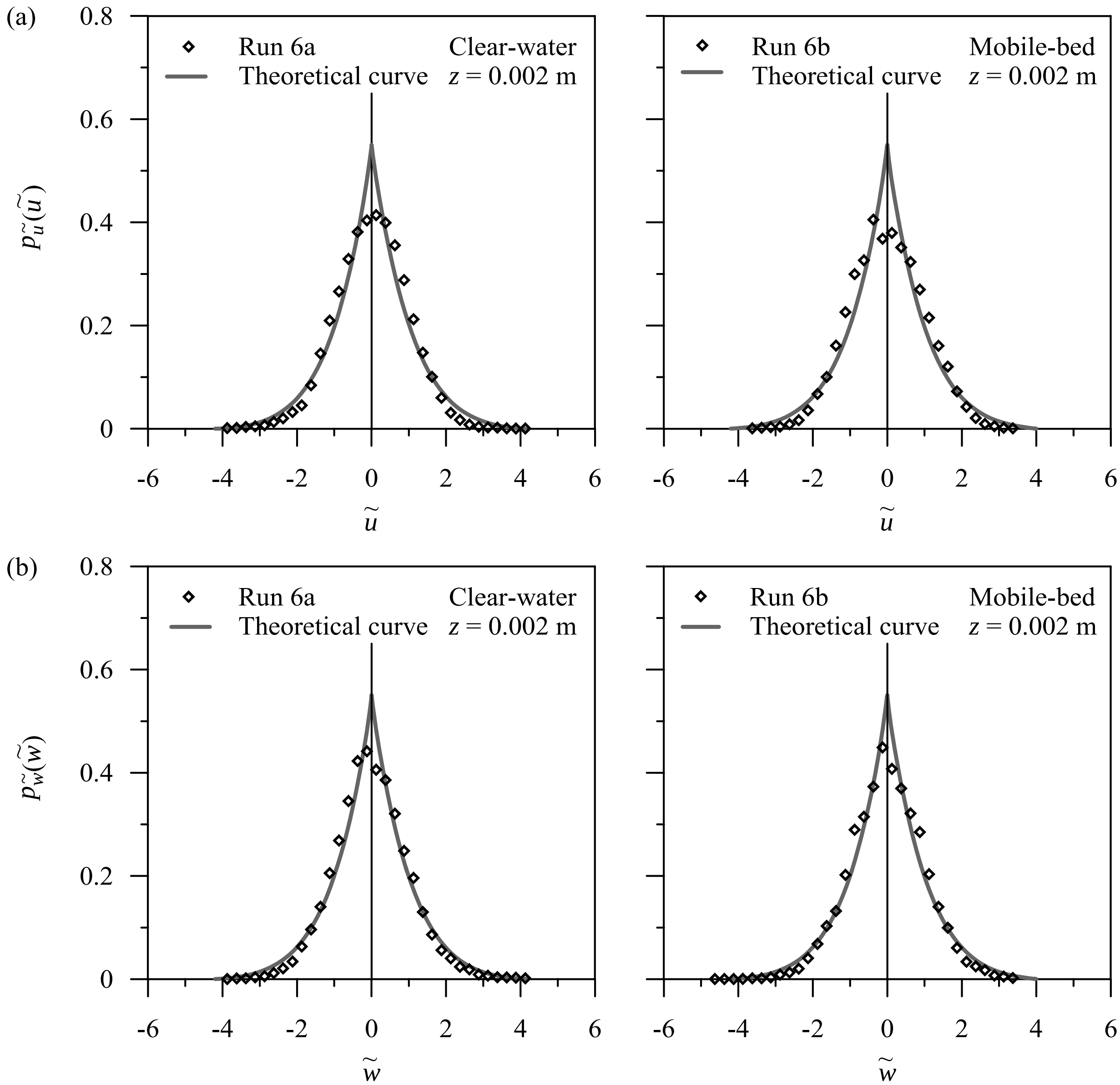

Fig. 13. Comparisons of computed (a) $p_{\tilde{u}}(\tilde{u})$ and (b) $p_{\tilde{w}}(\tilde{w})$ with experimental data for clear-water and mobile-bed cases.

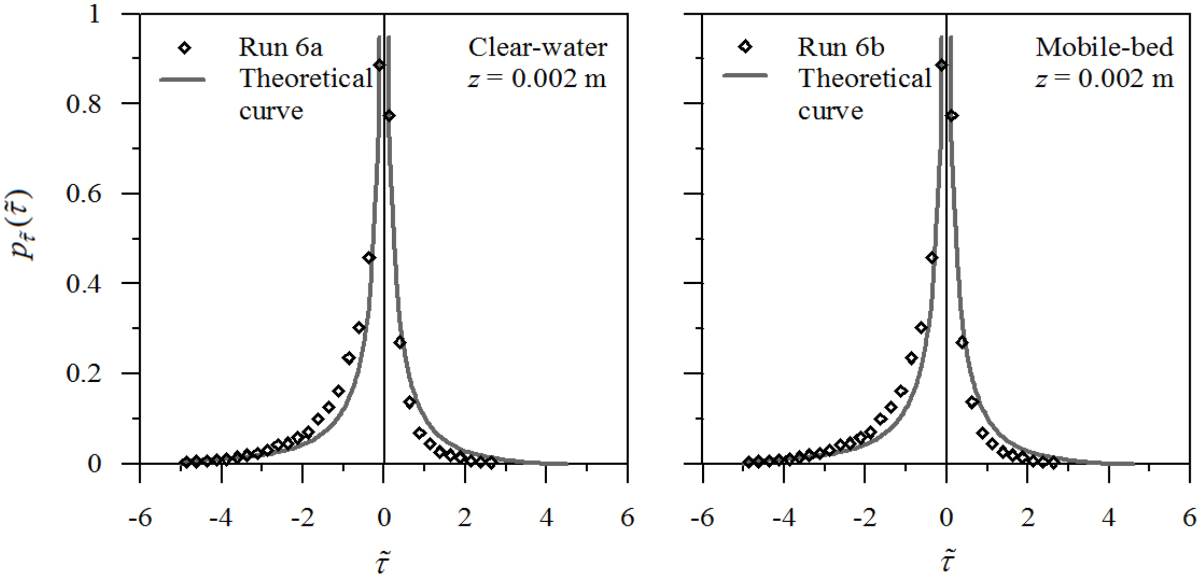

Fig. 14. Comparisons of computed $p_{\tilde{\tau}}(\tilde{\tau})$ with experimental data for clear-water and mobile-bed cases.

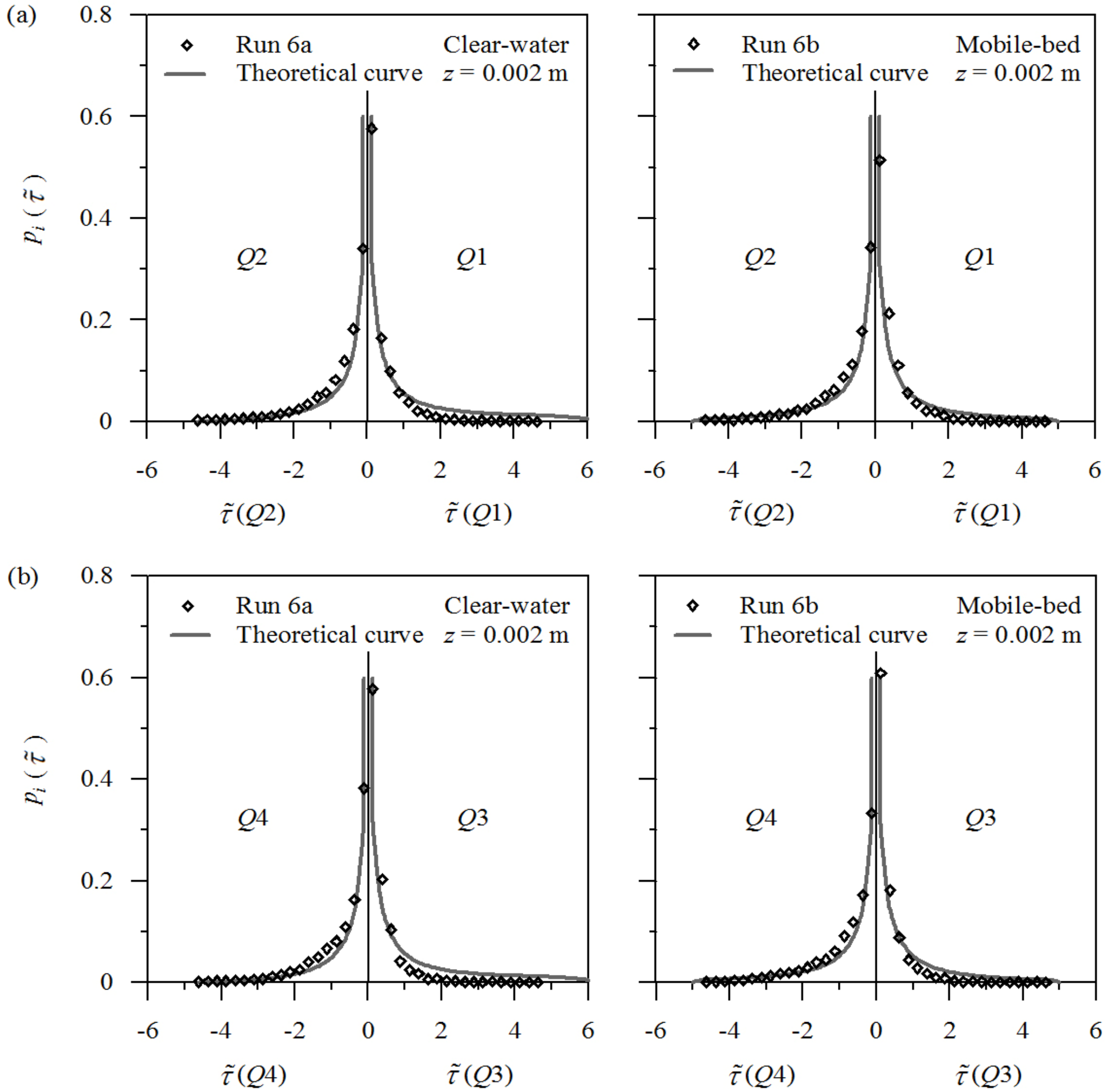

Fig. 15. Comparisons of computed (a) $p_{1,2}(\tilde{\tau})$ and (b) $p_{3,4}(\tilde{\tau})$ with experimental data for clear-water and mobile-bed cases.

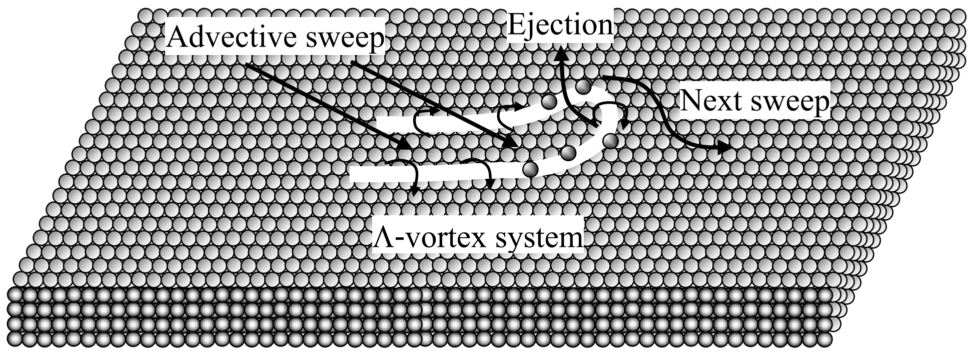

Fig. 16. Schematic of coherent structure during bed-load sediment transport.

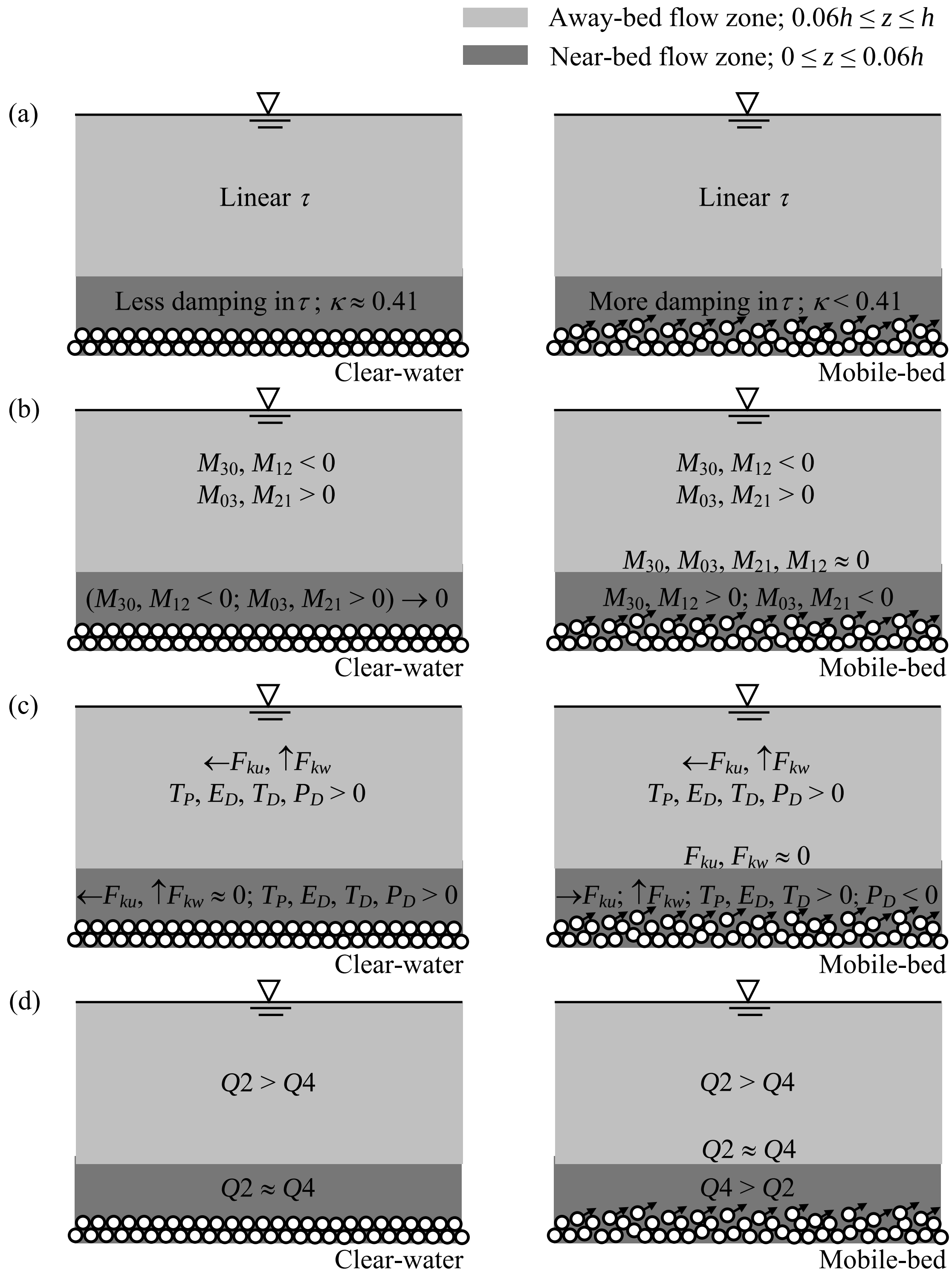

Fig. 17. Schematic close-up of the predominating turbulence parameters in near-bed and away-bed flow zones for clear-water and mobile-bed cases: (a) RSS, (b) third-order correlations, (c) TKE-flux components and budget and (d) bursting events for clear-water and mobile-bed flows.